Linear stability of a contaminated fluid flow down a slippery inclined plane

Farooq Ahmad Bhat and Arghya Samanta
Department of Applied Mechanics, Indian Institute of Technology Delhi, Hauz Khas, New Delhi 110016, India

(Received 16 March 2018; published 7 September 2018)

The linear stability analysis of a fluid flow down a slippery inclined plane is carried out when the free surface of the fluid is contaminated by a monolayer of insoluble surfactant. The aim is to extend the earlier study [Samanta *et al.*, J. Fluid Mech. **684**, 353 (2011)] for low to high values of the Reynolds number in the presence of an insoluble surfactant. The Orr-Sommerfeld equation (OSE) is derived for infinitesimal disturbances of arbitrary wave numbers. At low Reynolds number, the OSE is solved analytically by using the long-wave analysis, which shows that the critical Reynolds number decreases in the presence of a slippery plane but increases in the presence of an insoluble surfactant. This fact ensures a destabilizing effect of wall slip and a stabilizing effect of insoluble surfactant on the long-wave surface mode. Further, the Chebyshev spectral collocation method is implemented to tackle the OSE equation numerically for an arbitrary value of the Reynolds number, or equivalently, for an arbitrary value of the wave number. At moderate Reynolds number, wall slip exhibits a stabilizing effect on the surface mode as opposed to the result in the long-wave regime, while the insoluble surfactant exhibits a stabilizing effect on the surface mode as in the result of the long-wave regime. On the other hand, at high Reynolds number, both wall slip and insoluble surfactant exhibit a stabilizing effect on the shear mode. Further, it is shown that both surface and shear modes compete with each other to dominate the primary instability once the inclination angle is sufficiently small. In addition, new phase boundaries are identified to differentiate the regimes of surface and shear modes.

DOI: 10.1103/PhysRevE.98.033108

I. INTRODUCTION

There are numerous theoretical and experimental studies of falling film instability over the past few decades since the work of Kapitza [1] because of its prevalence in chemical and technological processes. For instance, the generation of instability on the surface of a coating film degrades the quality of the final product and thereby, the controlling process of that instability is of great practical interest [2]. Further, the wave formation at the film surface significantly enhances heat and mass transfer rates and, indeed, it plays a crucial role in the process equipment, such as falling film evaporators, condensers, and absorption columns [3,4]. Besides their applications, such studies are of special importance due to their relevance in the fundamental problems of fluid mechanics. In fact, instabilities often originate on the free surface to some flow conditions and undergo a transition to spatiotemporal chaos [5,6].

The linear stability analysis of a falling film down an inclined plane was initiated by Benjamin [7] and Yih [8] who explored the surface mode in detail at low Reynolds number. In particular, such mode is detected on the surface when the Reynolds number exceeds its critical value, $\mathrm{Re}_c = (5/4)\cot\theta$, where θ is the inclination angle. Later, the same problem was extended by Lin [9] and De Bruin [10] to decipher the shear mode which is often detected on the surface at high Reynolds number as soon as the inclination angle is sufficiently small. As discussed by De Bruin [10], the surface and shear modes compete with each other to dominate the primary instability at sufficiently small values of the inclination angle. This problem was further revisited by Chin *et al.* [11] and Floryan *et al.* [12] to take into account the effects of surface tension and inclination angle on the shear mode. According to their report, the critical Reynolds number corresponding to the shear mode displays a nonmonotonic behavior in the presence of surface tension.

In many practical situations, the solid substrate is not completely wetting [13], and this fact raises the question on the choice of no-slip boundary condition at the fluid-solid boundary [14,15]. Apart from that, the recent development of microfluidic and nanofluidic devices shows the existence of the slip effect at the fluid-solid boundary. Furthermore, the macroscopic modeling of the transport phenomena at the fluid-porous interface reveals a semiempirical Navier-slip boundary condition as long as the flow in the porous layer is driven by Darcy's equations [16,17]. In this context, Pascal [18] showed that a linear stability analysis of a two-sided fluid flow over a saturated porous inclined plane can be modeled into a linear stability analysis of a one-sided fluid flow over a slippery inclined plane. Later, the same study was expanded by Sadiq and Usha [19] and Thiele *et al.* [20] in the weak nonlinear regime to take into account the effect of nonlinearity. In fact, these studies were limited to the vicinity of the critical Reynolds number. Recently, the study proposed by Pascal [18] was further revisited by Samanta *et al.* [21] to explore the effect of slip boundary condition on the primary and secondary instabilities in the moderate Reynolds number regime. As mentioned by Samanta *et al.* [21], the slip length exhibits a dual role on the primary instability, i.e., a destabilizing effect close to the threshold of instability and a stabilizing effect far from the threshold of instability. However, there was no investigation into the high Reynolds number regime, which

provokes us for further exploration of the effect of slip length on the shear mode when the Reynolds number is quite large.

On the other hand, in order to delay the transition process of the surface instability to the spatiotemporal chaos, the insoluble surfactant or the soluble surfactant was incorporated in the model of falling film down an inclined plane by Whitaker and Jones [22], Ji and Setterwall [23], Pozrikidis [24], Blyth and Pozrikidis [25], Wei [26,27], and Karapetsas and Bontozoglou [28,29]. It was shown that the critical Reynolds number increases in the presence of an insoluble surfactant, i.e., the surfactant has a stabilizing effect on the surface mode. Recently, this model was extended by Anjalaiah *et al.* [30] by including the slippery plane instead of an impermeable plane. However, their study was confined to the moderate Reynolds number regime. No result regarding the shear mode was demonstrated in the high Reynolds number regime. In the present article, our aim is to fill those gaps available in the previous studies, i.e., to decipher the linear stability of a surfactant-laden film flown down a slippery inclined plane in different regimes of the Reynolds number. The results are produced in detail when the flow parameters vary.

II. EQUATIONS OF MOTION

Consider a gravity-driven viscous incompressible two-dimensional fluid flown down a slippery inclined plane having an angle θ with the horizontal line as sketched in Fig. 1. Suppose that the free surface $y = h(x,t)$ of the fluid is covered by an insoluble surfactant with concentration $\Gamma(x,t)$. The origin is located at the plane and the coordinate axes x and y are placed along the streamwise and crosswise flow directions, respectively. The physical properties, such as density ρ and dynamic viscosity μ are constants for a given fluid. The present flow configuration is governed by the mass and momentum conservation equations [6]

$$\partial_x u + \partial_y v = 0, \tag{1}$$

$$\rho(\partial_t + u\partial_x + v\partial_y)u = -\partial_x p + \mu(\partial_{xx} + \partial_{yy})u + \rho g \sin\theta, \tag{2}$$

$$\rho(\partial_t + u\partial_x + v\partial_y)v = -\partial_y p + \mu(\partial_{xx} + \partial_{yy})v - \rho g \cos\theta, \tag{3}$$

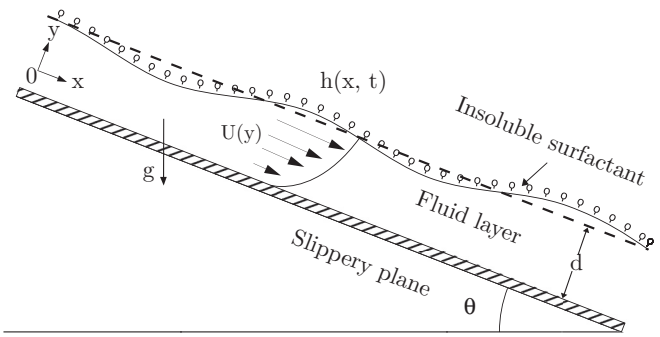

FIG. 1. Schematic diagram of a surfactant-laden fluid flow down a slippery inclined plane.

where u and v are velocity components and p is the pressure of the fluid. Here g is the gravitational acceleration. The system is subject to the following boundary conditions. At the plane $y = 0$ the velocity of the fluid satisfies Navier-slip and no penetration boundary conditions [18–21]

$$u = \alpha\partial_y u, \quad v = 0, \tag{4}$$

where α is the dimensional slip length of the slippery plane, which varies with the material property of the slippery plane. For example, the experimental measurement of slip length for a polydimethylsiloxane slippery plane is 250 μm [31]. At the free surface $y = h(x,t)$ the hydrodynamic stress is balanced by the Marangoni stress induced due to the transport of insoluble surfactant and yields the dynamic boundary conditions [24,25,32]

$$[4\mu\partial_y v\partial_x h + \mu(\partial_y u + \partial_x v)(1 - \partial_x h^2)] = (\partial_x\sigma + \partial_x h\partial_y\sigma)\sqrt{1 + \partial_x h^2}, \tag{5}$$

$$-p + \frac{2\mu}{[1 + \partial_x h^2]}[\partial_y v(1 - \partial_x h^2) - (\partial_y u + \partial_x v)\partial_x h] = \frac{\sigma\partial_{xx}h}{[1 + \partial_x h^2]^{3/2}}, \tag{6}$$

where σ is the surface tension of the fluid, which varies linearly with the surfactant concentration $\Gamma(x,t)$ through the following relation:

$$\sigma = \sigma_0 - E(\Gamma - \Gamma_0), \tag{7}$$

where σ_0 is the base surface tension corresponding to the base surfactant concentration Γ_0. The surface elasticity $E = -\partial_\Gamma\sigma|_{\Gamma=\Gamma_0} > 0$, because the surface tension of a fluid reduces with increasing value of the surfactant concentration. Further, the transport of insoluble surfactant at the free surface is described by the convection-diffusion equation [33–36]

$$\partial_t[\Gamma\sqrt{1 + \partial_x h^2}] + \partial_x[\Gamma u\sqrt{1 + \partial_x h^2}] = D_s\partial_x[\partial_x\Gamma/\sqrt{1 + \partial_x h^2}], \tag{8}$$

where D_s is the surfactant diffusivity. In practice, D_s is usually small. It should be useful to mention here that the insoluble surfactant moves with the same velocity as the fluid particle lying on the free surface. Finally, the kinematics of the free surface is described by the kinematic boundary condition

$$\partial_t h + u\partial_x h = v. \tag{9}$$

As we are interested in exploring the linear stability analysis, it is necessary to compute the base flow solution, which can be obtained by considering a unidirectional parallel flow with a constant fluid layer thickness $y = d$ and a constant surfactant concentration $\Gamma = \Gamma_0$. Consequently, the governing equations (1)–(9) are simplified in the following form:

$$\mu\partial_{yy}u + \rho g \sin\theta = 0, \quad \partial_y p + \rho g \cos\theta = 0, \tag{10}$$

$$u|_{y=0} = \alpha\partial_y u|_{y=0}, \quad \partial_y u|_{y=d} = 0, \quad p|_{y=d} = 0. \tag{11}$$

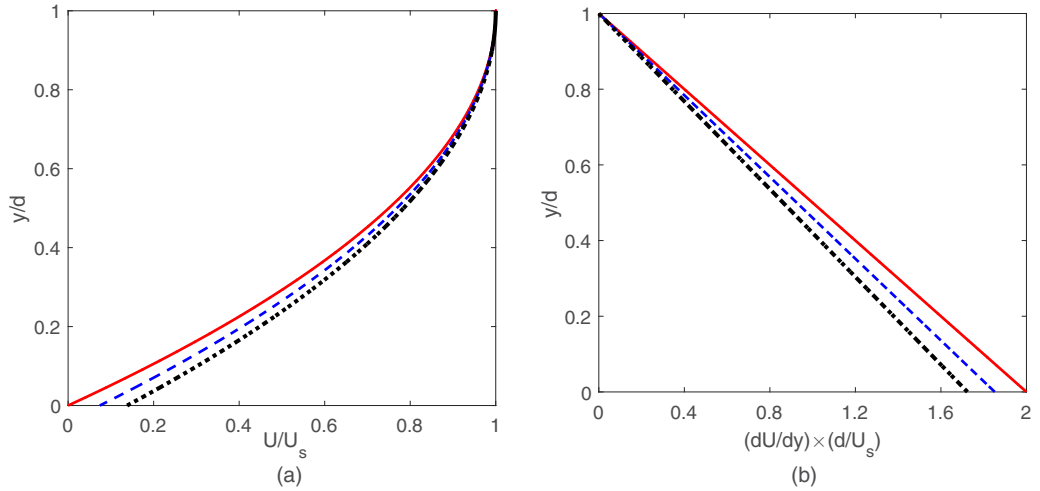

FIG. 2. (a) The variation of the streamwise base velocity U/U_s as a function of y/d. (b) The variation of the shear stress $(dU/dy) \times (d/U_s)$ as a function of y/d. Here solid, dashed, and dotted lines stand for $\beta = 0$, $\beta = 0.04$, and $\beta = 0.08$, respectively.

The solution of the base equations (10) and (11) can be expressed as

$$U(y) = \frac{\rho g d^2 \sin\theta}{2\mu}\left(2\frac{y+\alpha}{d} - \frac{y^2}{d^2}\right), \tag{12}$$

$$P(y) = \rho g d \cos\theta\left(1 - \frac{y}{d}\right) \tag{13}$$

and the associated flow rate can be expressed as

$$Q = \int_0^d U(y)dy = \frac{\rho g d^3 \sin\theta}{\mu}\left(\frac{1}{3} + \frac{\alpha}{d}\right). \tag{14}$$

In fact, the maximum value of the streamwise base velocity appears at the free surface and its magnitude is given by $U_s = [\rho g d^2 \sin\theta/(2\mu)](1+2\beta)$, where $\beta = \alpha/d$ is the dimensionless slip length whose reasonable range is $(0 - 0.08)$ for a fluid with base layer thickness $d = 3\times10^{-3}$ m [37]. Obviously, the base velocity is independent of the surfactant concentration. Figure 2(a) demonstrates that the streamwise base velocity enhances in the presence of slip length. On the contrary, the wall shear stress reduces in the presence of slip length, which can be found in Fig. 2(b). This result ensures that base flow velocity is strongly influenced by the slippery plane.

A. Dimensionless criterion

The above set of governing equations (1)–(9) are made dimensionless by choosing d as the characteristic length scale, U_s as the characteristic velocity scale, ρU_s^2 as the pressure scale, σ_0 as the scale for surface tension, and Γ_0 as the scale for surfactant concentration. After normalizing, the governing equations are written in the nondimensional form

$$\partial_x u + \partial_y v = 0, \tag{15}$$

$$\mathrm{Re}(\partial_t u + u\partial_x u + v\partial_y u + \partial_x p) = \partial_{xx}u + \partial_{yy}u + 2/(1+2\beta), \tag{16}$$

$$\mathrm{Re}(\partial_t v + u\partial_x v + v\partial_y v + \partial_y p) = \partial_{xx}v + \partial_{yy}v - 2\cot\theta/(1+2\beta), \tag{17}$$

where $\mathrm{Re} = \rho U_s d/\mu$ is the Reynolds number which compares the inertia force with the viscous force. Similarly, after normalizing, the associated boundary conditions are written in the nondimensional form

$$u = \beta\partial_y u, \quad v = 0, \quad \text{at} \quad y = 0, \tag{18}$$

$$[4\partial_y v\partial_x h + (\partial_y u + \partial_x v)(1 - \partial_x h^2)] = -(\mathrm{Ma}/\mathrm{Ca})\partial_x\Gamma\sqrt{1+\partial_x h^2}, \quad \text{at} \quad y = h, \tag{19}$$

$$-\mathrm{Re}\, p + \frac{2}{[1+\partial_x h^2]}[\partial_y v(1-\partial_x h^2) - (\partial_y u + \partial_x v)\partial_x h] = \frac{[1-\mathrm{Ma}(\Gamma-1)]\partial_{xx}h}{\mathrm{Ca}[1+\partial_x h^2]^{3/2}}, \quad \text{at} \quad y = h, \tag{20}$$

$$\partial_t[\Gamma\sqrt{1+\partial_x h^2}] + \partial_x[\Gamma u\sqrt{1+\partial_x h^2}] = (1/\mathrm{Pe})\partial_x[\partial_x\Gamma/\sqrt{1+\partial_x h^2}], \quad \text{at} \quad y = h, \tag{21}$$

$$\partial_t h + u\partial_x h = v, \quad \text{at} \quad y = h, \tag{22}$$

where $\mathrm{Ma} = E\Gamma_0/\sigma_0$ is the Marangoni number which compares the Marangoni stress with the surface stress, $\mathrm{Ca} = \mu U_s/\sigma_0$ is the capillary number which compares the viscous stress with the surface stress, and $\mathrm{Pe} = U_s d/D_s$ is the Péclet number which compares the advective mass transport and the diffusive mass transport of an insoluble surfactant at the free surface.

B. Perturbation equations

Consider an infinitesimal disturbance on the base flow, and accordingly, each flow variable can be decomposed as

$$z = Z + z', \tag{23}$$

where Z represents the base flow variables and z' represents the perturbation flow variables. Substituting equation (23) in the dimensionless governing equations (15)–(22) and linearizing with respect to the base solution, we obtain perturbation equations

$$\partial_x u' + \partial_y v' = 0, \tag{24}$$

$$\mathrm{Re}(\partial_t u' + U\partial_x u' + v'\partial_y U + \partial_x p') - \partial_{xx}u' - \partial_{yy}u' = 0, \tag{25}$$

$$\mathrm{Re}(\partial_t v' + U\partial_x v' + \partial_y p') - \partial_{xx} v' - \partial_{yy} v' = 0, \quad (26)$$

$$[u' - \beta\partial_y u']|_{y=0} = 0, \quad v'|_{y=0} = 0, \quad (27)$$

$$[\partial_y u' + \partial_x v' + h'\partial_{yy} U]|_{y=1} + (\mathrm{Ma}/\mathrm{Ca})\partial_x \Gamma' = 0, \quad (28)$$

$$[-\mathrm{Re}\, p' + \{2\cot\theta/(1+2\beta)\}h' + 2\partial_y v']|_{y=1} - (1/\mathrm{Ca})\partial_{xx} h' = 0, \quad (29)$$

$$\partial_t \Gamma' + U|_{y=1}\partial_x \Gamma' + \partial_x u'|_{y=1} - (1/\mathrm{Pe})\partial_{xx}\Gamma' = 0, \quad (30)$$

$$\partial_t h' + U|_{y=1}\partial_x h' - v'|_{y=1} = 0. \quad (31)$$

III. ORR-SOMMERFELD EQUATION

Now the perturbation stream function ψ' is introduced from the perturbation continuity equation (24) by the following relation:

$$u' = \partial_y \psi', \quad v' = -\partial_x \psi'. \quad (32)$$

Inserting equation (32) into the perturbation momentum equations (25) and (26) and eliminating pressure terms from those equations, we obtain a fourth-order partial differential equation (PDE) in terms of ψ'

$$(\partial_{yyyy}\psi' + 2\partial_{xxyy}\psi' + \partial_{xxxx}\psi') = \mathrm{Re}[(\partial_{tyy}\psi' + \partial_{txx}\psi') + U(\partial_{xyy}\psi' + \partial_{xxx}\psi') - \partial_x\psi'\partial_{yy}U]. \quad (33)$$

Next the solution of the perturbation equations (24)–(31) is assumed in the normal mode form [8]

$$\psi'(x,y,t) = \phi(y)\exp[ik(x-ct)], \quad (34)$$

$$h'(x,t) = \eta\exp[ik(x-ct)], \quad (35)$$

$$\Gamma'(x,t) = \gamma\exp[ik(x-ct)], \quad (36)$$

where k is the wavenumber and $c = c_r + ic_i$ is the complex wave speed of the infinitesimal disturbance. Here ϕ, η and γ are respectively the amplitude of stream function, deformation of the free surface and perturbation surfactant concentration. It should be noted that the perturbation stream function $\psi'(x,y,t)$, surface deformation $h'(x,t)$ and perturbation surfactant concentration $\Gamma'(x,t)$ are all in the same phase. After substitution of the normal mode solution (34)–(36) in PDE (33), one can obtain a usual form of the Orr-Sommerfeld (OS) equation

$$(\partial_{yyyy} - 2k^2\partial_{yy} + k^4)\phi = \mathrm{Re}\, ik[(U-c)(\partial_{yy} - k^2) - \partial_{yy}U]\phi. \quad (37)$$

Similarly, using the normal mode solution (34)–(36), the perturbation boundary conditions (27)–(31) can be recast into the following form

$$\phi = 0, \quad (\partial_y\phi - \beta\partial_{yy}\phi) = 0, \quad \text{at} \quad y = 0, \quad (38)$$

$$(\partial_{yy} + k^2)\phi + \eta\partial_{yy}U + (\mathrm{Ma}/\mathrm{Ca})ik\gamma = 0, \ \text{at}\ y = 1, \quad (39)$$

$$(\partial_{yyy} - 3k^2\partial_y)\phi - ik\mathrm{Re}(U-c)\partial_y\phi - ik[\{2\cot\theta/(1+2\beta)\} + k^2/\mathrm{Ca}]\eta = 0, \ \text{at}\ y = 1, \quad (40)$$

$$\partial_y\phi + (U-c)\gamma - (1/\mathrm{Pe})ik\gamma = 0, \ \text{at}\ y = 1, \quad (41)$$

$$\phi + (U-c)\eta = 0, \ \text{at}\ y = 1. \quad (42)$$

Equations (37)–(42) are sometimes called the Orr-Sommerfeld eigenvalue problem, where c is the eigenvalue. In fact, the real part c_r of the eigenvalue c is the phase speed of the disturbance while the imaginary part c_i, or equivalently, kc_i is the growth rate of the disturbance. If $c_i > 0$, the infinitesimal disturbance will grow with time and becomes unstable. On the other hand, if $c_i < 0$, the infinitesimal disturbance will decay with time and becomes stable. $c_i = 0$ leads to the neutral stability criterion.

A. Solution of OS equation at inertialess approximation without surfactant

In the inertialess approximation ($\mathrm{Re} \to 0$), the Orr-Sommerfeld equation (37) is simplified into a fourth-order homogeneous ordinary differential equation with constant coefficients

$$\partial_{yyyy}\phi - 2k^2\partial_{yy}\phi + k^4\phi = 0. \quad (43)$$

The general solution of (43) is of the form

$$\phi(y) = (a_1 + a_2 y)e^{ky} + (a_3 + a_4 y)e^{-ky}, \quad (44)$$

where a_1, a_2, a_3, and a_4 are integrating constants to be determined from the boundary conditions. Putting the solution (44) in the boundary conditions (38)–(42) and setting $\mathrm{Re} = 0$, we obtain a set of five homogeneous linear equations in terms of a_1, a_2, a_3, a_4 and η. In fact, this set of equations are useful to study from a matrix point of view and thereby, these equations are transformed into a matrix form

$$\mathcal{M}\mathcal{X} = 0, \quad (45)$$

where $\mathcal{M}$ is a 5×5 square matrix and $\mathcal{X}$ is a 5×1 column matrix defined by

$$\mathcal{M} = \begin{pmatrix} 1 & 0 & 1 & 0 & 0 \\ (k^2\beta - k) & 2k\beta - 1 & (k^2\beta + k) & -2k\beta - 1 & 0 \\ e^k k^2 & e^k(k^2+k) & e^{-k}k^2 & e^{-k}(k^2-k) & -1/(2\beta+1) \\ -2e^k k^3 & -2e^k k^3 & 2e^{-k}k^3 & 2e^{-k}k^3 & -ik[2\cot\theta/(2\beta+1) + (k^2/\mathrm{Ca})] \\ e^k & e^k & e^{-k} & e^{-k} & 1-c \end{pmatrix} \quad \text{and} \quad \mathcal{X} = \begin{pmatrix} a_1 \\ a_2 \\ a_3 \\ a_4 \\ \eta \end{pmatrix}.$$

Hence for a nontrivial solution of $\mathcal{X}$, the determinant of $\mathcal{M}$ must be zero, i.e.,

$$\det(\mathcal{M}) = 0, \quad (46)$$

which leads to a dispersion relation corresponding to the inertialess flow configuration over a slippery plane. The phase speed c_r and the growth rate kc_i are determined from the dispersion relation and expressed as

$$c_r = 1 + \frac{2}{1 + 2(1+2\beta)k^2 + 2k\beta\ \sinh 2k + \cosh 2k} \tag{47}$$

and

$$kc_i = \frac{[\cot\theta + \{k^2(1+2\beta)/(2\mathrm{Ca})\}][(2+2\beta)k - 2\beta k\ \cosh 2k - \sinh 2k]}{k(1+2\beta)[1 + 2(1+2\beta)k^2 + 2\beta k\ \sinh 2k + \cosh 2k]}. \tag{48}$$

The current results are in full agreement with that of Yih [8] and Samanta [38] when the slip length β vanishes. Further, there is evidence that the resulting growth rate is negative despite the presence of the slippery wall.

B. Solution of OS equation at low Reynolds number

In order to solve the Orr-Sommerfeld boundary value problem (OS BVP) (37)–(42) analytically at low Reynolds number, the long-wave regular perturbation technique ($k \to 0$) is used as proposed by Yih [8]. In this method, the amplitude of each perturbation field is expanded in the series form

$$\phi(y) = \sum_{n=0}^{\infty} \phi_n k^n, \quad \eta = \sum_{n=0}^{\infty} \eta_n k^n, \tag{49}$$

$$\gamma = \sum_{n=0}^{\infty} \gamma_n k^n, \quad c = \sum_{n=0}^{\infty} c_n k^n, \tag{50}$$

where $n \in \mathbb{N} \cup \{0\}$, and $\mathbb{N}$ is the set of natural numbers. After substitution of (49) and (50) in the OS BVP (37)–(42), we collect the leading order equations, i.e., $\mathcal{O}(k^0)$ equations

$$\partial_{yyyy}\phi_0 = 0, \tag{51}$$

$$\phi_0|_{y=0} = 0,\ [\partial_y\phi_0 - \beta\partial_{yy}\phi_0]|_{y=0} = 0, \tag{52}$$

$$[\partial_{yy}\phi_0 + \eta_0\partial_{yy}U]|_{y=1} = 0,\ \partial_{yyy}\phi_0|_{y=1} = 0, \tag{53}$$

$$[\partial_y\phi_0 + (U - c_0)\gamma_0]|_{y=1} = 0, \tag{54}$$

$$[\phi_0 + (U - c_0)\eta_0]|_{y=1} = 0. \tag{55}$$

The solution of the leading order equations (51)–(55) is given by

$$\phi_0(y) = \eta_0[2\beta y + y^2]/(1+2\beta). \tag{56}$$

Obviously, the leading order ϕ_0 strongly depends on the slip length, but it is free from the surfactant concentration. Inserting the expression of ϕ_0 in (54) and (55), we get a coupled system of algebraic equations in terms of η_0 and γ_0,

$$[2(1+\beta)/(1+2\beta)]\eta_0 - (c_0 - 1)\gamma_0 = 0, \tag{57}$$

$$(c_0 - 2)\eta_0 = 0. \tag{58}$$

In fact, Eqs. (57) and (58) reveal the existence of two modes as reported by Wei [26]. If $\eta_0 \neq 0$, the resulting mode is referred to as the surface mode because it describes the deviation of the free surface from the base flow solution. The leading order phase speed c_0 of the surface mode is given by

$$c_0 = 2 \tag{59}$$

and the leading order amplitude γ_0 of the surfactant concentration is given by

$$\gamma_0 = 2\eta_0[(1+\beta)/(1+2\beta)]. \tag{60}$$

It is noticed that the dimensional leading order phase speed of the surface mode is two times the velocity of the fluid particle at the free surface. In this case, the deflection of the free surface and the perturbation surfactant concentration always lie in the same phase because the slip length β is positive. In the absence of wall slip, the current result coincides with that of Wei [26] when the imposed shear stress is removed from the free surface. On the other hand, if $\eta_0 = 0$, the resulting mode is referred to as the surfactant mode because it is generated by the perturbation surfactant concentration. In this case, the leading order phase speed c_0 of the surfactant mode is given by

$$c_0 = 1, \tag{61}$$

provided the leading order amplitude of the surfactant concentration is nonzero, i.e., $\gamma_0 \neq 0$. Note that the dimensional leading order phase speed of the surfactant mode is exactly the same as the velocity of the fluid particle at the free surface. In other words, the surface mode travels faster than the surfactant mode. Now we collect the first-order equations, i.e., $\mathcal{O}(k)$ equations

$$\partial_{yyyy}\phi_1(y) - i\mathrm{Re}[(U - c_0)\partial_{yy} - \partial_{yy}U]\phi_0 = 0, \tag{62}$$

$$\phi_1|_{y=0} = 0,\ \ [\partial_y\phi_1 - \beta\partial_{yy}\phi_1]|_{y=0} = 0, \tag{63}$$

$$[\partial_{yy}\phi_1 + \eta_1\partial_{yy}U]|_{y=1} + i(\mathrm{Ma}/\mathrm{Ca})\gamma_0 = 0, \tag{64}$$

$$[\partial_{yyy}\phi_1 - i\,\mathrm{Re}(U - c_0)\partial_y\phi_0]|_{y=1} - [2i\cot\theta/(1+2\beta)]\eta_0 = 0, \tag{65}$$

$$[\partial_y\phi_1 + (U - c_0)\gamma_1]|_{y=1} - c_1\gamma_0 - (1/\mathrm{Pe})i\gamma_0 = 0, \tag{66}$$

$$\phi_1 + (U - c_0)\eta_1 - c_1\eta_0 = 0. \tag{67}$$

The solution of the first-order equations (62)–(67) is given by

$$\phi_1(y) = b_1 y + b_2 y^2 + b_3 y^3 + b_4 y^4 + b_5 y^5, \tag{68}$$

where

$$b_1 = -\frac{2i\,\mathrm{Re}\beta(1 + 4\beta + 6\beta^2)\eta_0}{3(1+2\beta)^2} - \frac{2i\beta(\cot\theta\eta_0 + i\eta_1)}{1+2\beta} - i\beta\{(\mathrm{Ma}/\mathrm{Ca})\gamma_0 - c_0\mathrm{Re}\eta_0\},$$

$$b_2 = (1/2\beta)b_1,$$

$$b_3 = i\eta_0\left[\frac{\cot\theta}{3(1+2\beta)} + \frac{2\beta^2\mathrm{Re}}{3(1+2\beta)^2} - \frac{\beta c_0\mathrm{Re}}{3(1+2\beta)}\right],$$

$$b_4 = \frac{i\,\mathrm{Re}}{6(1+2\beta)}\left[\frac{\beta}{1+2\beta} - \frac{c_0}{2}\right]\eta_0,$$
$$b_5 = \frac{i\,\mathrm{Re}(1+\beta)\eta_0}{30(1+2\beta)^2}.$$

Substituting the expression of ϕ_1 in Eqs. (66) and (67), we get a coupled system of algebraic equations in terms of η_0, η_1, γ_0, and γ_1,

$$i\left[\mathrm{Re}\left\{\frac{2\left(1+3\beta+3\beta^2\right)c_0}{3(1+2\beta)}\right\} - \cot\theta - \mathrm{Re}\left\{\frac{3+15\beta+28\beta^2+24\beta^3}{6(1+2\beta)^2}\right\}\right]\eta_0 + \left[\frac{2+2\beta}{1+2\beta}\right]\eta_1$$
$$-[(i/\mathrm{Pe}+c_1)+i(1+\beta)(\mathrm{Ma}/\mathrm{Ca})]\gamma_0 + (1-c_0)\gamma_1 = 0, \tag{69}$$

$$\left[\frac{i\,\mathrm{Re}(5+20\beta+24\beta^2)c_0}{12(1+2\beta)} - c_1 - \frac{2i(1+3\beta)\cot\theta}{3(1+2\beta)} - \frac{i}{10}\left\{\frac{\mathrm{Re}\left(3+18\beta+40\beta^2+40\beta^3\right)}{(1+2\beta)^2}\right\}\right]\eta_0$$
$$+(2-c_0)\eta_1 - [i(1/2+\beta)(\mathrm{Ma}/\mathrm{Ca})]\gamma_0 = 0. \tag{70}$$

Hence, for the surface mode we must have $\eta_0 \neq 0$. Using the expression of γ_0 and $c_0 = 2$ in (70), one can obtain the expression for c_1

$$c_1 = -i[d_1(\mathrm{Ma}/\mathrm{Ca}) + d_2\mathrm{Re} + d_3\cot\theta], \tag{71}$$

where

$$d_1 = (\beta+1),$$
$$d_2 = -4(1+\beta)[2+5\beta(2+3\beta)]/[15(1+2\beta)^2],$$
$$d_3 = [2(1+3\beta)]/[3(1+2\beta)].$$

The difference with the expression of c_1 reported by Anjalaiah *et al.* [30] can be attributed to the choice of the distinct velocity scale. In the absence of wall slip, the expression of c_1 is identical with that of Blyth and Pozrikidis [25] and Wei [26]. The criterion $c_1 = 0$ leads to the analytical expression of critical Reynolds number corresponding to the surfactant-laden falling film down a slippery inclined plane

$$\mathrm{Re}_c = \frac{15(1+2\beta)^2(\mathrm{Ma}/\mathrm{Ca})}{4(15\beta^2+10\beta+2)} + \frac{5(2\beta+1)(3\beta+1)\cot\theta}{30\beta^3+50\beta^2+24\beta+4}. \tag{72}$$

Indeed, the critical Reynolds number is independent of the Péclet number. Therefore, the surface mode will be unstable to an infinitesimal long-wave disturbance if $\mathrm{Re} > \mathrm{Re}_c$. Otherwise, it will be stable if $\mathrm{Re} < \mathrm{Re}_c$. Note that the critical Reynolds number is significantly affected by the slip length. In fact, Re_c decreases monotonically in a linear fashion with the increasing value of the slip length, which can be found in Fig. 3. Further, the above critical Reynolds number recovers the result of Samanta *et al.* [21] very well when the free surface is uncontaminated from an insoluble surfactant ($\mathrm{Ma} \to 0$)

$$\mathrm{Re}_c = (5\cot\theta/4)\frac{(1+2\beta)(1+3\beta)}{[(15/2)\beta^3+(25/2)\beta^2+6\beta+1]}.$$

In addition, Re_c recovers the result of Blyth and Pozrikidis [25] and Wei [26] very well when the slip length vanishes ($\beta \to 0$):

$$\mathrm{Re}_c = (5\cot\theta/4) + (15/8)(\mathrm{Ma}/\mathrm{Ca}).$$

On the other hand, for the surfactant mode we have $\eta_0 = 0$ and $c_0 = 1$, which yield

$$\eta_1 = i[\mathrm{Ma}(1+2\beta)]\gamma_0/(2\mathrm{Ca}), \tag{73}$$
$$c_1 = -i/\mathrm{Pe}. \tag{74}$$

In this case, c_1 depends on the Péclet number Pe, and it is completely negative. This fact indicates that the surfactant mode will be damped to an infinitesimal long-wave disturbance. It

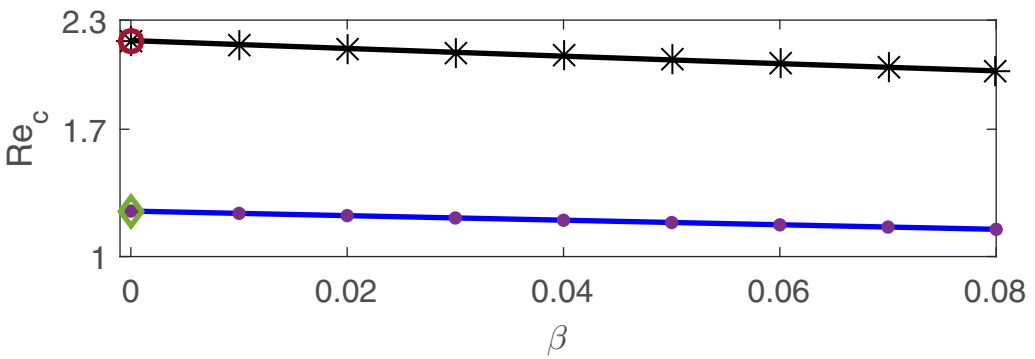

FIG. 3. The variation of the critical Reynolds number Re_c for the surface mode with the slip length β when $\mathrm{Ma} = 1$, $\mathrm{Ca} = 2$, and $\theta = \pi/4$. The stars connected by straight line segments represent the present result. The circle is the result of Blyth and Pozrikidis [25]. The solid points connected by the blue line segments are the results of Samanta *et al.* [21] without surfactant, and the green diamond is the result of Yih [8].

TABLE I. Comparison between the analytical and numerical values of the critical Reynolds number for the surface mode when the slip length varies. Here $\theta = \pi/4$, Ca $= 2$, Pe $= 2$, and Ma $= 1$.

Comparison	$\beta = 0$	$\beta = 0.04$	$\beta = 0.08$
Analytical ($\mathrm{Re_c}$)	2.1875	2.1017	2.0209
Numerical ($\mathrm{Re_c}$)	2.1875	2.1018	2.0210

should be noted that Eq. (73) is exactly a balance between the perturbation shear stress $\eta_1 \partial_{yy} U$ and the Marangoni stress $i(\mathrm{Ma}/\mathrm{Ca})\gamma_0$. In this case, the first-order $[\mathcal{O}(k)]$ perturbation flow $\phi(1)$ becomes zero, which is consistent with the result because the surfactant mode is generated due to the deflection of the perturbation surfactant concentration.

IV. SOLUTION OF OS EQUATION FOR ARBITRARY REYNOLDS NUMBER

A. Solution of OS equation at moderate Reynolds number

In order to solve the OS equation for an arbitrary Reynolds number, or equivalently, for an arbitrary wave number, we use the Chebyshev spectral collocation method proposed by Schmid and Henningson [39]. Consequently, the OS BVP (37)–(42) are converted into a generalized matrix eigenvalue problem [40–42]

$$\mathcal{A}\phi = c\mathcal{B}\phi, \tag{75}$$

where c is the eigenvalue and ϕ is the associated eigenvector. The matrices $\mathcal{A}$ and $\mathcal{B}$ can be expressed as

$$\mathcal{A} = -\frac{1}{i\,\mathrm{Re}}(D^4 - 2k^2D^2 + k^4) + kU(D^2 - k^2) - kD^2U,$$
$$\mathcal{B} = k(D^2 - k^2), \quad D = d/dy.$$

The eigenvalue problem (75) is closed by applying the boundary conditions given in (38)–(42). In fact, in the Chebyshev spectral collocation method, the amplitude function ϕ is expanded in a truncated series of Chebyshev polynomials

$$\phi = \sum_{i=0}^{N} \phi_i T_i(y), \tag{76}$$

where N is the number of Chebyshev polynomials and ϕ_i's are unknown coefficients to be determined from the numerical simulation. As the Chebyshev polynomials $T_i(y)$ are defined over the domain $[-1, 1]$, the liquid layer domain $[0, 1]$ is shifted to $[-1, 1]$ by applying a transformation $y = (x + 1)/2$. As a result, the derivatives are replaced by $D \to 2D$, $D^2 \to 4D^2$, … . Inserting (76) into the eigenvalue problem (75), the Chebyshev functions are evaluated at the Gauss-Lobatto collocation points $x_j = \cos(\pi j/N)$, which are extrema of the Chebyshev polynomials, where $j = 0, \ldots, N$. First of all, the present numerical code is verified by comparing the numerical and long-wave analytical results. Accordingly, both results are demonstrated in Tables I and II, respectively. Indeed, there exists an excellent match between the numerical and analytical results.

To take into account the individual effect of slip length on the surface mode in the moderate Reynolds number regime,

TABLE II. Comparison between the analytical and numerical values of the critical Reynolds number for the surface mode when the Marangoni number varies. Here $\theta = \pi/4$, Ca $= 2$, Pe $= 2$, and $\beta = 0$.

Comparison	Ma $= 0$	Ma $= 1$	Ma $= 2$	Ma $= 3$
Analytical ($\mathrm{Re_c}$)	1.2500	2.1875	3.1250	4.0625
Numerical ($\mathrm{Re_c}$)	1.2498	2.1875	3.1251	4.0626

these flow parameters $\theta = \pi/4$, Ca $= 2$, Pe $= 2$, and Ma $= 1$ are kept constant except slip length. The neutral curve for the surface mode is computed numerically for several values of the slip length and displayed in Fig. 4(a). Basically, such curves are obtained from the numerical experiment when the imaginary part of the most unstable eigenvalue corresponding to the surface mode vanishes. Note that two different scenarios of instability are manifested in the neutral diagram as predicted by Samanta *et al.* [21] in the context of an uncontaminated film flow over a slippery inclined plane. In the vicinity of the threshold of instability, wall slip shows a destabilizing effect [see inset of Fig. 4(a)], but it shows a stabilizing effect far from the threshold. In other words, wall slip plays a dual role on the primary instability. This result is further justified through the temporal growth rate kc_i (when $k \in \mathbb{R}$ and $c \in \mathbb{C}$, $\mathbb{R}$ is the set of real numbers, and $\mathbb{C}$ is the set of complex numbers) of an infinitesimal disturbance. Thereby, we choose two distinct Reynolds numbers from the destabilizing and stabilizing zones, respectively, and compute the temporal growth rate numerically for different values of the slip length. Indeed, the temporal growth rate corresponding to the surface

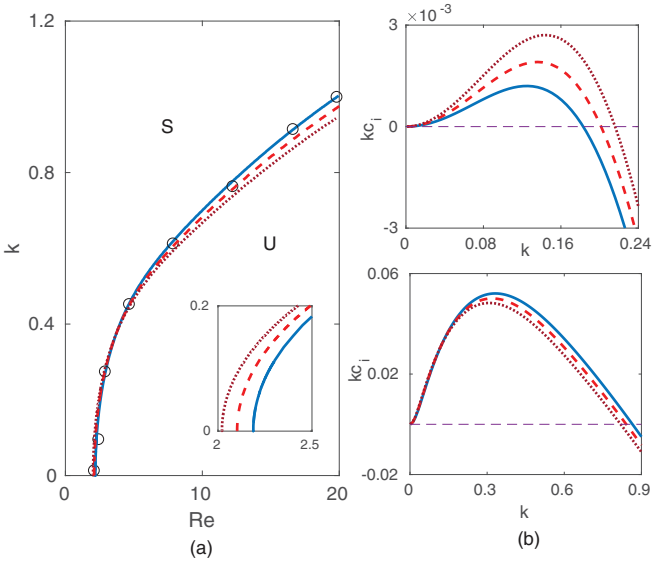

FIG. 4. (a) The variation of the neutral curve for the surface mode in the (Re, k) plane for different values of the slip length when $\theta = \pi/4$, Ca $= 2$, Pe $= 2$, and Ma $= 1$. Here "U" and "S" indicate unstable and stable regions, respectively. (b) The variation of the temporal growth rate kc_i for the surface mode with wave number k when Re $= 2.5$ (top) and Re $= 15$ (bottom). Here solid, dashed, and dotted lines stand for $\beta = 0$, $\beta = 0.04$, and $\beta = 0.08$, respectively. The circles show the results of Blyth and Pozrikidis [25].

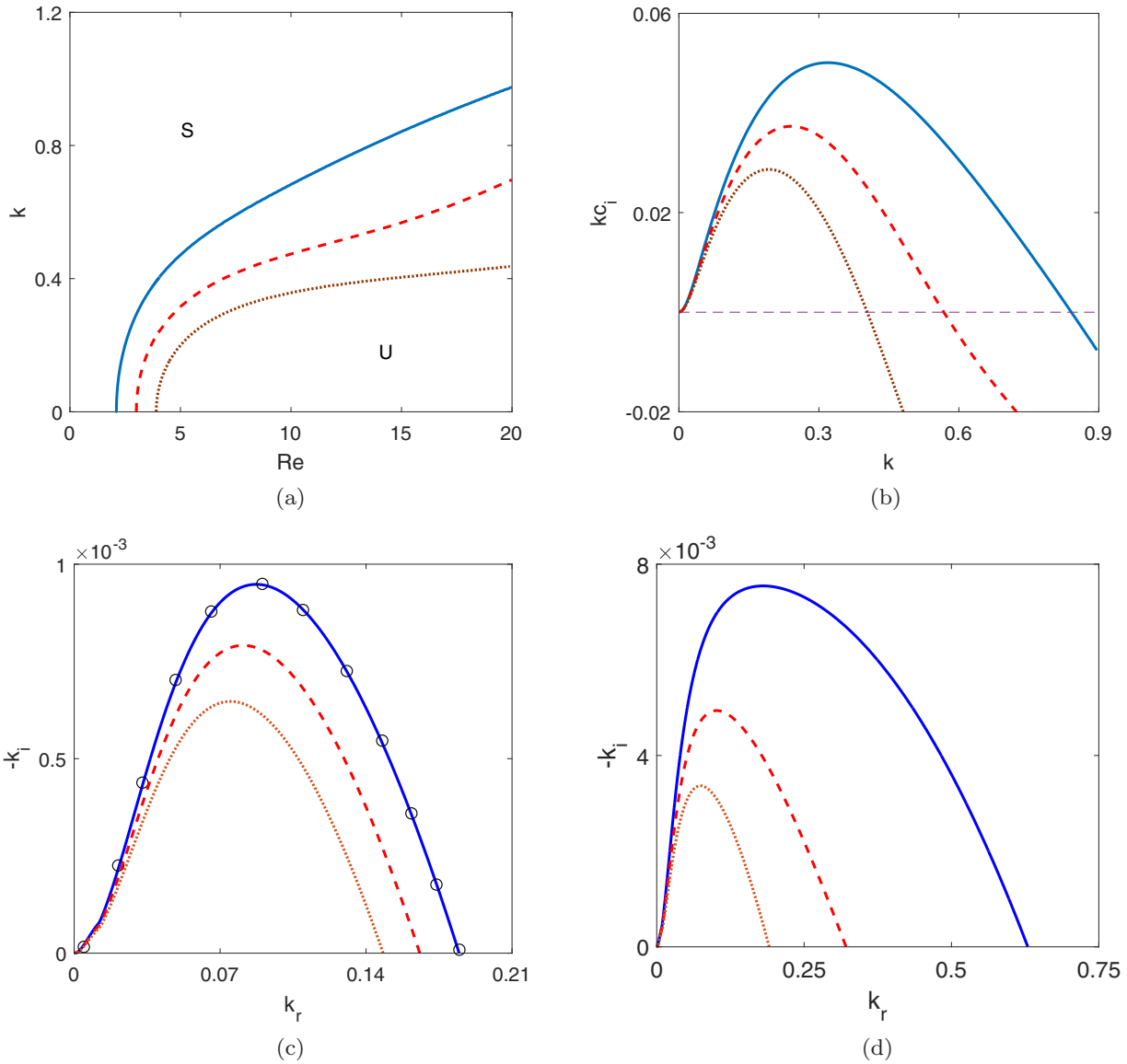

FIG. 5. (a) The variation of the neutral curve for the surface mode in the (Re, k) plane for different values of the Marangoni number when $\theta = \pi/4$, $\mathrm{Ca} = 2$, $\mathrm{Pe} = 2$, and $\beta = 0.04$. Here "U" and "S" indicate unstable and stable regions, respectively. (b) The variation of the temporal growth rate kc_i for the surface mode with wave number k when $\mathrm{Re} = 15$. Here solid, dashed, and dotted lines stand for $\mathrm{Ma} = 1$, $\mathrm{Ma} = 2$, and $\mathrm{Ma} = 3$, respectively. (c) The variation of the spatial growth rate $-k_i$ for the surface mode with the wave number k_r when $\theta = 4^\circ$, $\beta = 0$, $\mathrm{Ka} = 13.3$, and $\mathrm{Re} = 20$. Here solid, dashed, and dotted lines stand for $\mathrm{Ma} = 0$, $\mathrm{Ma} = 0.05$, and $\mathrm{Ma} = 0.1$, respectively. The circles are the results of Samanta *et al.* [21]. (d) The variation of the spatial growth rate $-k_i$ for the surface mode with the wave number k_r when $\theta = 4^\circ$, $\beta = 0$, $\mathrm{Ka} = 13.3$, and $\mathrm{Re} = 40$. Here solid, dashed, and dotted lines stand for $\mathrm{Ma} = 0$, $\mathrm{Ma} = 1$, and $\mathrm{Ma} = 2$, respectively.

mode intensifies [see Fig. 4(b), top] in the destabilizing zone but attenuates [see Fig. 4(b), bottom] in the stabilizing zone with the increasing value of the slip length. This fact is fully consistent with the results reported in Fig. 4(a). In particular, the flow rate or equivalently, the Reynolds number enhances with the increasing value of the slip length and causes a destabilizing effect close to the onset of instability. On the other hand, for a fixed value of the Reynolds number, the base film thickness reduces to compensate the effect of slip length, which strengthens the impact of the capillary term on the primary instability far from the onset region and leads to a stabilizing effect.

To take into account the individual effect of the Marangoni number on the surface mode, the neutral curve for the surface mode is computed numerically for several values of the Marangoni number when the other flow parameters $\theta = \pi/4$, $\mathrm{Ca} = 2$, $\mathrm{Pe} = 2$, and $\beta = 0.04$ are fixed. The ensuing results are displayed in Fig. 5(a). Note that the unstable region reduces significantly with the increasing value of the Marangoni number. This result ensures the stabilizing effect of the Marangoni number on the primary instability. As discussed by Frenkel and Halpern [33], Halpern and Frenkel [34], Blyth and Pozrikidis [43], and Wei [26], the surfactant concentration is higher in the crest region in comparison with

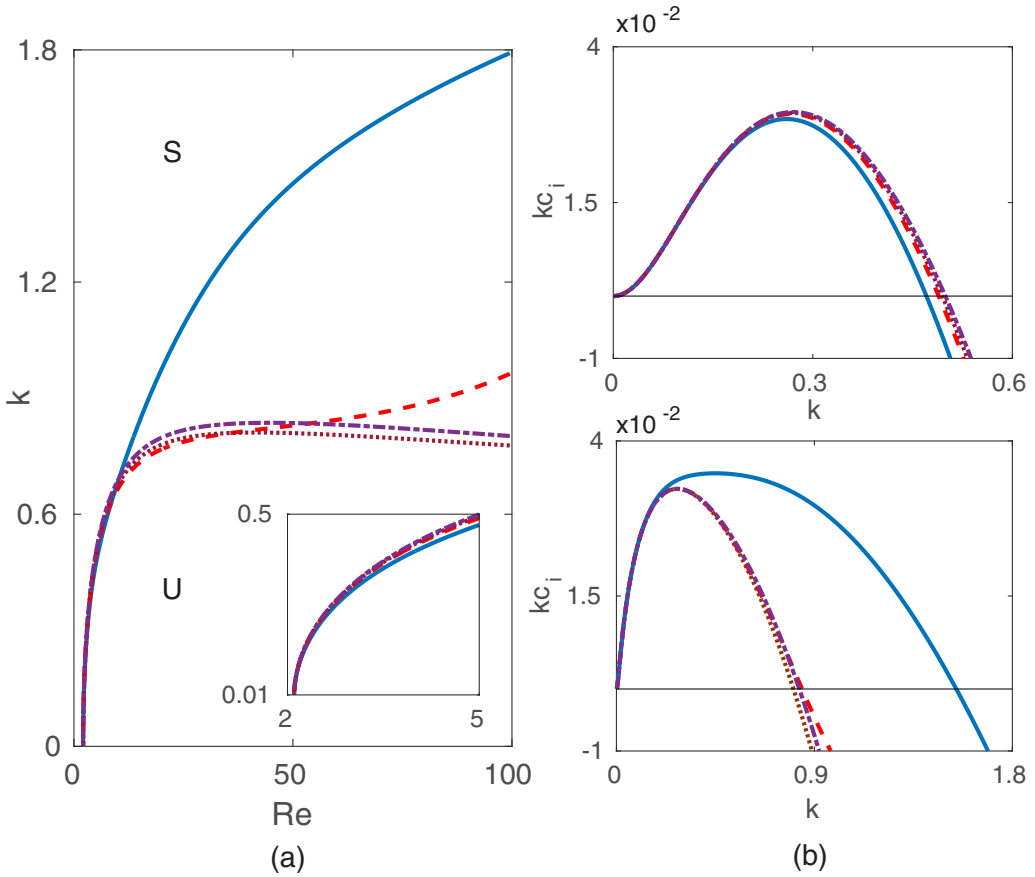

FIG. 6. (a) The variation of the neutral curve for the surface mode in the (Re, k) plane for different values of the Péclet number when $\theta = \pi/4$, Ca $= 2$, Ma $= 1$, and $\beta = 0.04$. Here solid, dashed, dotted, and dash-dotted lines stand for Pe $= 2$, Pe $= 10$, Pe $= 20$, and Pe $= 100$, respectively. Here "U" and "S" indicate unstable and stable regions, respectively. (b) The variation of the temporal growth rate kc_i for the surface mode with wave number k when Re $= 5$ (top). The variation of the temporal growth rate kc_i for the surface mode with wave number k when Re $= 60$ (bottom). Here solid, dashed, dotted, and dash-dotted lines stand for Pe $= 2$, Pe $= 10$, Pe $= 20$, and Pe $= 100$, respectively.

the trough region of a deformed free surface because the surface deformation and the perturbation surfactant concentration are in the same phase. Therefore, a local flow induced by the Marangoni traction generates from the crest toward the trough and leads to a stabilizing effect on the primary instability. However, if the surface deformation and the perturbation surfactant concentration are out of phase, then the surfactant concentration is higher in the trough region in comparison with the crest region of a deformed free surface. Therefore, a local flow induced by the Marangoni traction generates from the trough toward the crest and leads to a destabilizing effect [26,33,34,43]. This result is further justified through the temporal growth rate kc_i of an infinitesimal disturbance and depicted in Fig. 5(b). Indeed, the temporal growth rate corresponding to the surface mode attenuates in the presence of an insoluble surfactant, which is consistent with the result reported in Fig. 5(a). Furthermore, this result is strengthened by producing the spatial growth rate $-k_i$ (when $c \in \mathbb{R}$ and $k \in \mathbb{C}$) for several values of the Marangoni number when Re $= 20$ and Re $= 40$. Therefore, we require the complex input for the wave number k in the numerical experiment rather than the real input used to compute the temporal growth rate. The spatial growth rate for the surface mode is depicted in Figs. 5(c) and 5(d), respectively, for a silicon oil with Ka $= 13.3$, where Ka $= \mathrm{Re}^{2/3}[(1+2\beta)/2]^{1/3}/\mathrm{Ca}$, the Kapitza number, depends on the physical properties of a given fluid. Note that the spatial growth rate also attenuates with the increasing value of the Marangoni number, which indicates the stabilizing effect of the Marangoni number on the surface mode. In addition, the spatial growth rate recovers the result of Samanta *et al.* [21] very well in the limit Ma $\to 0$.

To take into account the individual effect of the Péclet number on the surface mode, the neutral curve for the surface mode is computed numerically for several values of the Péclet number when the other flow parameters $\theta = \pi/4$, Ca $= 2$, Ma $= 1$, and $\beta = 0.04$ are fixed. The results can be found in Fig. 6(a). Obviously, all neutral curves emerge from the critical Reynolds number as $k \to 0$, which supports the analytical expression of the critical Reynolds number given in (72). In fact, the critical Reynolds number does not depend on Pe. It is noteworthy to point out that the Péclet number also exhibits a dual role on the primary instability as predicted by the slip length. The unstable region enhances in the vicinity of the critical Reynolds number [see inset of Fig. 6(a)] but reduces far from the critical Reynolds number with the increasing value of the Péclet number. In addition, there occurs a significant reduction of the unstable region far from the criticality

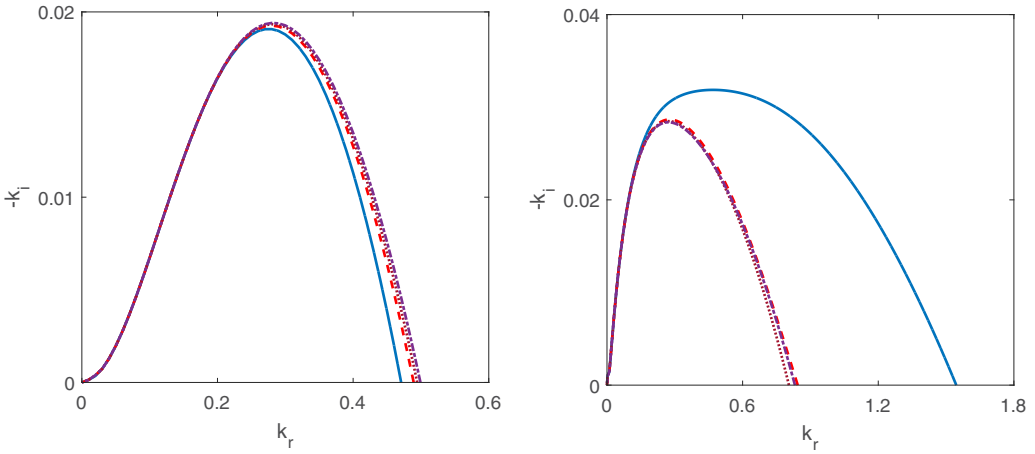

FIG. 7. (a) The variation of the spatial growth rate $-k_i$ for the surface mode with the wave number k_r when $\theta = \pi/4$, $\beta = 0.04$, Ca $= 2$, Ma $= 1$, and Re $= 5$. Here solid, dashed, dotted, and dash-dotted lines stand for Pe $= 2$, Pe $= 10$, Pe $= 20$, and Pe $= 100$, respectively. (b) The variation of the spatial growth rate $-k_i$ for the surface mode with the wave number k_r when $\theta = \pi/4$, $\beta = 0.04$, Ca $= 2$, Ma $= 1$, and Re $= 60$. Here solid, dashed, dotted, and dash-dotted lines stand for Pe $= 2$, Pe $= 10$, Pe $= 20$, and Pe $= 100$, respectively.

as soon as the Péclet number switches from Pe $= 2$ to Pe $=$ 10. However, if Pe is enlarged continuously after that, the unstable region no longer reduces significantly. It seems that the impact of the Péclet number, or equivalently, the impact of surfactant diffusivity approaches a saturation limit. At the free surface, surfactant diffuses due to the presence of a diffusive term in the transport equation (8). In particular, surfactant diffuses from the higher concentration regime (crest regime) to the lower concentration regime (trough regime). Therefore, if Pe exists in the transport equation, the surfactant diffuses from the crest regime to the trough regime and inhibits the Marangoni flow, which results in a destabilizing effect. Now, if Pe is enlarged continuously, the surfactant diffusive effect becomes negligible, which supports the Marangoni flow from the crest regime toward the trough regime of a deformed free surface and leads to a stabilizing effect. For this reason, the unstable region initially decreases with the increasing value of the Péclet number, but it almost remains the same at high value of the Péclet number (Pe $\geqslant 10$). These results are further justified through the temporal growth rate kc_i of an infinitesimal disturbance. Consequently, we select two values of the Reynolds number Re $= 5$ and Re $= 60$ from the destabilizing and stabilizing zones, respectively. The temporal growth rate for the surface mode is computed numerically for different values of the Péclet number and displayed in Fig. 6(b). Indeed, the temporal growth rate enhances at Re $=$ 5 but attenuates at Re $= 60$ with the increasing value of the Péclet number and supports the results reported in Fig. 6(a), i.e., the temporal growth rate increases close to the criticality but decreases far from the criticality and almost remains the same at the high value of the Péclet number (Pe $\geqslant 10$). This result is further strengthened by producing the spatial growth rate $-k_i$ corresponding to the surface mode for several values of the Péclet number when Re $= 5$ and Re $= 60$. The ensuing results are displayed in Figs. 7(a) and 7(b), respectively. Note that the spatial growth rate also follows the same trend as predicted by the temporal growth rate with the increasing value of the Péclet number, which ensures the dual behavior of the Péclet number on the surface mode.

B. Convergence of spectrum

In this section, we check convergence for the spectrum as determined by the eigenvalue problem (75) when the flow parameters vary. To this end, the relative error is introduced as proposed by Tilton and Cortelezzi [44] and Samanta [37]:

$$E_N = \|\boldsymbol{c}_{N+1} - \boldsymbol{c}_N\|_2 / \|\boldsymbol{c}_N\|_2, \tag{77}$$

where $\|\cdot\|_2$ specifies the L_2 norm. In particular, the relative error E_N is computed numerically by considering 20 least stable eigenvalues and illustrated in Fig. 8. It is observed that the relative error for all different cases (see Fig. 8) approximately saturates in the range $[\mathcal{O}(10^{-7}), \mathcal{O}(10^{-5})]$ for $N \geqslant 80$ when Re $= 10^4$, $k = 1$, and $\theta = 4^\circ$ are fixed. This fact implies that the accurate numerical result can be achieved as long as the number of Chebyshev polynomials in the series expansion (76) is greater than or equal to 80. Further, the spectrum of the eigenvalue problem (75) is displayed in Fig. 9 for different values of the slip length as well as for different values of the Marangoni number. In the first case, the slip length is varied while the other parameters are fixed. If $\beta = 0$, the most unstable mode appears at $c = 0.156\,646\,89 + i0.005\,054\,89$ when Re $= 21\,000$, $k = 1.2$, $\theta = 1' = (1^\circ/60)$, Ka $= 51\,269.45$, and Ma $= 0$ [12]. However, the most unstable mode shifts to $c = 0.183\,050\,73 + i0.000\,329\,76$ if $\beta = 0.03$. Obviously, c_i, or equivalently, the growth rate decays with β and thereby, one can expect the stabilizing effect of slip length on the shear mode. In the second case, the Marangoni number is varied while the other parameters are fixed. If Ma $= 0$, the most unstable mode appears at $c = 0.191\,431\,97 + i0.000\,821\,54$ when Re $= 7000$, $k = 2.3$, $\theta = 1'$, Ka $= 51269.45$, and $\beta = 0$. However, the most unstable mode shifts to $c = 0.191\,568\,66 + i0.000\,220\,69$ at Ma $= 20$. Obviously, c_i, or equivalently, the growth rate decreases with Ma and thereby, in the second case also, one can expect the stabilizing effect of the Marangoni number on the shear mode.

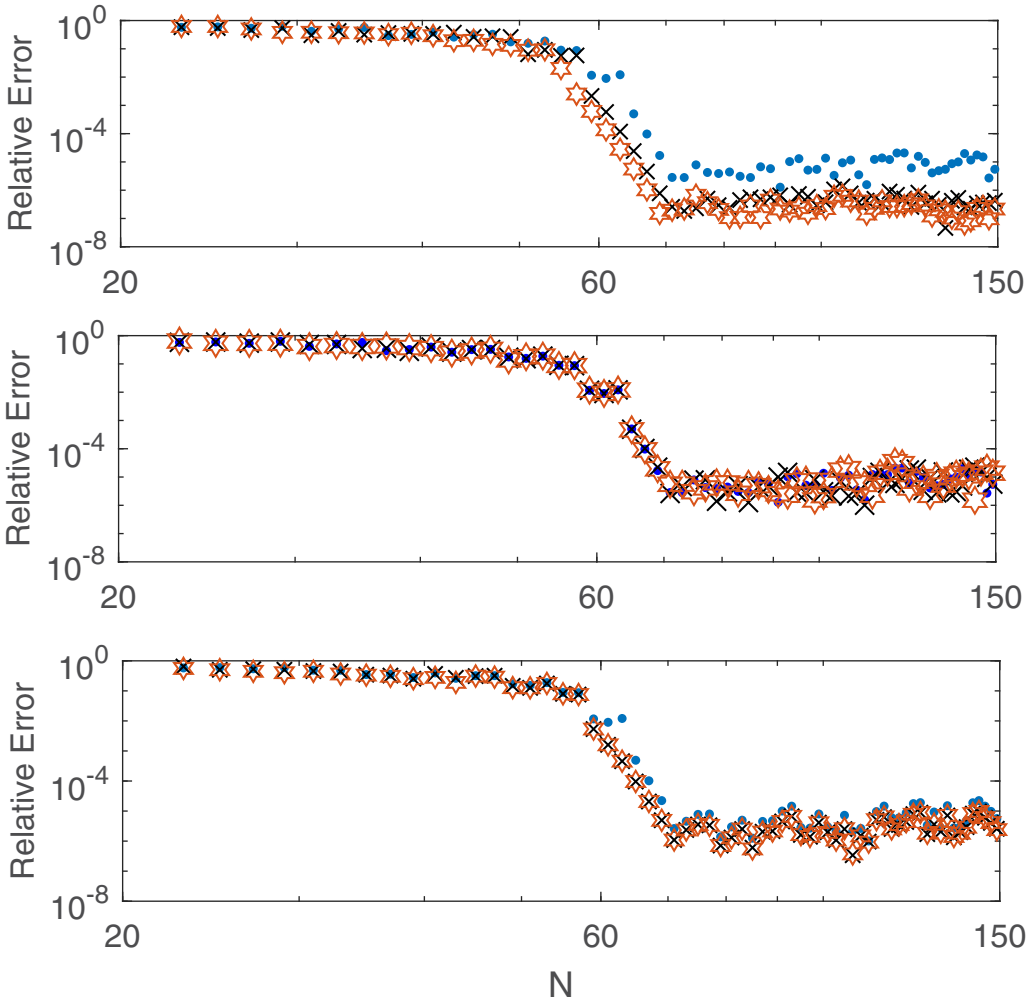

FIG. 8. The variation of the relative error E_N with the number of Chebyshev polynomials N when $\theta = 4^\circ$, Ca $= 2$, Re $= 10^4$, and $k = 1$. (Top) Solid, cross, and star points stand for $\beta = 0$, $\beta = 0.04$, and $\beta = 0.08$, respectively, when Ma $= 0$ and Pe $= 2$. (Middle) Solid, cross, and star points stand for Ma $= 0$, Ma $= 1$, and Ma $= 3$, respectively, when $\beta = 0$ and Pe $= 2$. (Bottom) Solid, cross, and star points stand for Pe $= 2$, Pe $= 10$, and Pe $= 20$, respectively, when $\beta = 0$ and Ma $= 1$.

C. Effect of slip length on the shear mode

In order to decipher an independent effect of slip length on the shear mode, the numerical experiment is carried out for large values of the Reynolds number. In particular, the shear mode is detected in the numerical experiment when the inclination angle is very small. To take into account this fact, the results are produced for a water flow with $\theta = 1^\circ$, Ka $=$ 13 096.3, and Ma $= 0$ [11]. Figure 10(a) illustrates the neutral curve for the shear mode in the (Re, k) plane for different values of the slip length. It should be noticed that the unstable region corresponding to the shear mode decreases significantly with the increasing value of the slip length, which is followed by the successive amplification of the critical Reynolds number. The result can be found in the inset of Fig. 10(a). Further, this result is strengthened by producing the temporal growth rate kc_i corresponding to the shear mode as shown for a surface mode in the previous Sec. IV A. Consequently, a Reynolds number Re $=$ 15 000 is selected from the unstable zone and the temporal growth rate for the shear mode is computed numerically when the slip length varies. As soon as the slip length is enlarged, the temporal growth rate attenuates significantly with the slip length [see Fig. 10(b)] and supports the result reported in Fig. 10(a). There is evidence that the temporal growth rate fully disappears from the unstable zone at $\beta = 0.027$. Therefore, one can conclude that the slip length has a stabilizing effect on the shear mode. This result also agrees with the behavior of the spectrum of the eigenvalue problem (75) where the temporal growth rate of the most unstable shear mode decays with the increasing value of the slip length (see Fig. 9). In addition, the present result is verified with that of Chin *et al.* [11] when the slip length vanishes ($\beta = 0$). Indeed, an excellent agreement is achieved.

D. Effect of Marangoni number on the shear mode

In order to decipher an independent effect of the Marangoni number on the shear mode, the numerical experiment is repeated for a water flow with $\theta = 1'$, Ka $=$ 51 269.45, and $\beta = 0$ [12]. The results are produced for different values of the Marangoni number when the other flow parameters are fixed. Figure 11(a) illustrates the neutral curve for the shear mode in the (Re, k) plane when the Marangoni

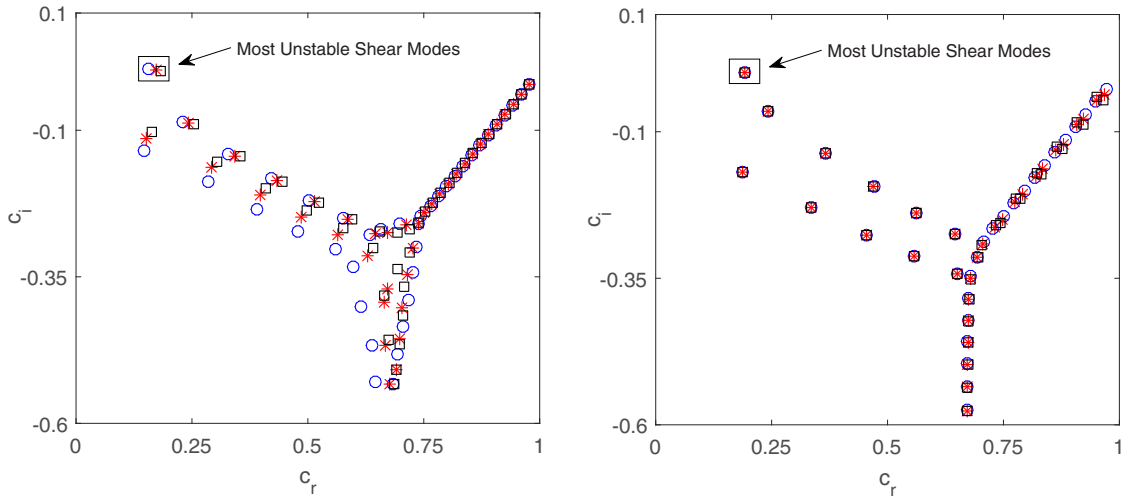

FIG. 9. (a) The spectrum of the eigenvalue problem (75) when Re = 21 000, $k = 1.2$, $\theta = 1'$, Ka = 51 269.45, and Ma = 0. Here circles, stars and squares represent the results of $\beta = 0$, $\beta = 0.02$, and $\beta = 0.03$, respectively. (b) The spectrum of the eigenvalue problem (75) when Re = 7000, $k = 2.3$, $\theta = 1'$, Ka = 51 269.45, and $\beta = 0$. Here circles, stars, and squares represent the results of Ma = 0, Ma = 10, and Ma = 20, respectively.

number varies. It should be noticed that the unstable region corresponding to the shear mode reduces with the increasing value of the Marangoni number when the inclination angle is very small, i.e., $\theta = 1'$. This fact is followed by the successive amplification of the critical Reynolds number, which is shown in the inset of Fig. 11(a). Therefore, one can predict that the Marangoni number has also a stabilizing influence on the shear mode when the inclination angle is sufficiently small. Further, this result is strengthened by determining the temporal growth rate kc_i corresponding to the shear mode. Accordingly, a Reynolds number Re = 7400 is selected from the unstable zone, and the ensuing temporal growth rate for the shear mode is computed numerically when the Marangoni number varies successively. Indeed, the temporal growth rate attenuates with the increasing value of the Marangoni number [see Fig. 11(b)] and supports the result reported in Fig. 11(a). This fact indicates the stabilizing effect of the Marangoni number on the shear mode. Further, there is evidence that the temporal growth rate completely diminishes from the unstable zone at Ma = 62. In addition, the present result captures the result of Floryan *et al.* [12] very well when the Marangoni number Ma is set to zero. From the above result we can also

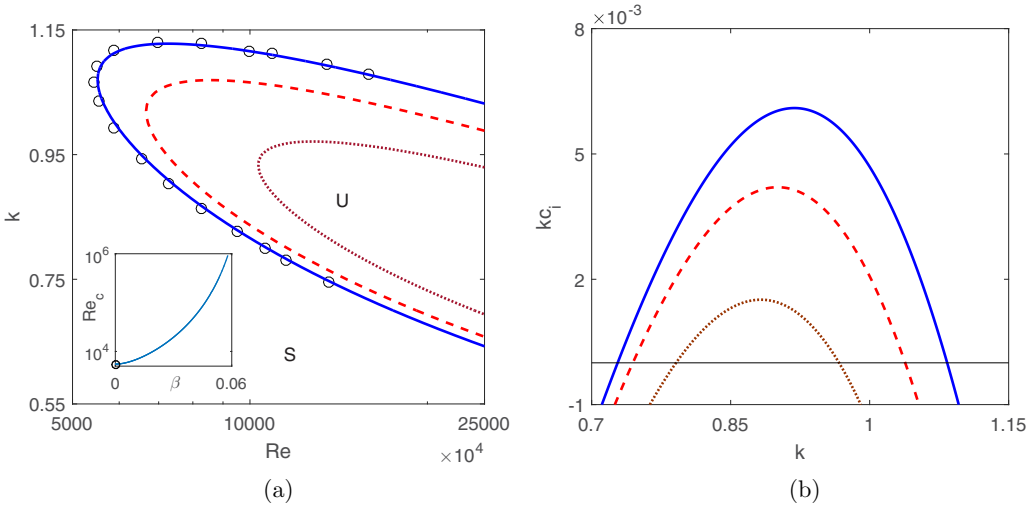

FIG. 10. (a) The variation of the neutral curve for the shear mode in the (Re, k) plane for different values of the slip length when $\theta = 1^\circ$, Ka = 13 096.3, and Ma = 0. Solid, dashed, and dotted lines stand for $\beta = 0$, $\beta = 0.01$, and $\beta = 0.02$, respectively. Here "U" and "S" indicate unstable and stable regions, respectively. The circles are the results of Chin *et al.* [11]. (b) The variation of the temporal growth rate kc_i for the shear mode with the wave number k when Re = 15 000. Solid, dashed, and dotted lines stand for $\beta = 0$, $\beta = 0.01$, and $\beta = 0.02$, respectively.

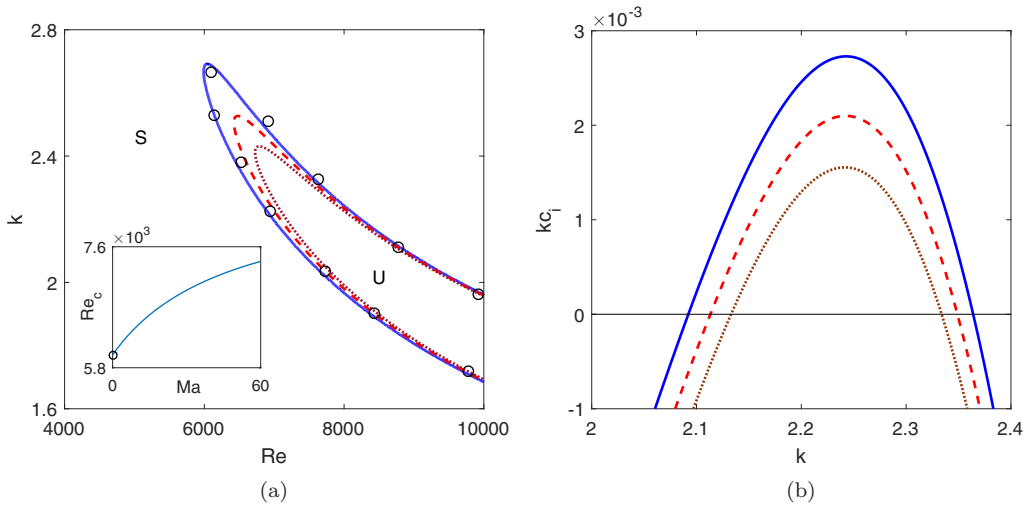

FIG. 11. (a) The variation of the neutral curve for the shear mode in the (Re, k) plane for different values of the Marangoni number when $\theta = 1'$, Ka $= 51\,269.45$, and $\beta = 0$. Solid, dashed, and dotted lines stand for Ma $= 0$, Ma $= 10$, and Ma $= 20$, respectively. Here "U" and "S" indicate unstable and stable regions, respectively. The circles are the results of Floryan *et al.* [12]. (b) The variation of the temporal growth rate kc_i for the shear mode with the wave number k when Re $= 7400$. Solid, dashed, and dotted lines stand for Ma $= 0$, Ma $= 10$, and Ma $= 20$, respectively.

conclude that the slip length has a stronger influence on the shear mode than that of the Marangoni number.

E. Effect of Péclet number on the shear mode

In order to decipher an independent effect of the Péclet number on the shear mode, the numerical experiment is performed again for large values of the Reynolds number when the inclination angle is very small. The results are computed for $\theta = 1'$, Ca $= 2$, $\beta = 0$, and Ma $= 1$. Figures 12(a) and 12(c) exhibit the neutral curve for the shear mode in the (Re, k) plane for different values of the Péclet number. It should be noticed that the results are produced beyond the reasonable range of the Péclet number to see its impact on the shear mode in the high Reynolds number regime. The reasonable range of the Péclet number is quite high even for the low viscous liquids. For the typical values of $U_s = 1$ m/s, $d = 10^{-3}$ m, $\nu = 10^{-6}$ m^2/s, and $D_s = 10^{-9}$ m^2/s, Re $\sim \mathcal{O}(10^3)$ and Pe $\sim \mathcal{O}(10^6)$ [46,47]. It is observed that the unstable region reduces with the Péclet number in the range Pe $\in [0, 3.5]$ approximately, which is followed by the successive amplification of the critical Reynolds number [see inset of Fig. 12(a)]. As soon as the Péclet number crosses the upper limit, the unstable region no longer reduces but eventually enhances with the Péclet number, and ultimately approaches a saturation domain. This fact is followed by the successive reduction of the critical Reynolds number. Finally, the critical Reynolds number approaches a saturation value $\mathrm{Re_c} = 5376$ approximately in a similar fashion as observed in the case of the unstable region at large Pe [see inset of Fig. 12(c)]. Obviously, the Péclet number exhibits a dual role on the shear mode as in the case of the surface mode. However, the result corresponding to the shear mode is completely opposite to that of the surface mode. Further, the above result is strengthened by producing the temporal growth rate kc_i corresponding to the shear mode as shown for the surface mode in the previous Sec. IV A. Consequently, we choose a Reynolds number Re $= 5450$ from the unstable zone and compute the temporal growth rate numerically when the Péclet number varies gradually. Indeed, the temporal growth rate for the shear mode attenuates with Pe in the range Pe $\in [0, 3.5]$ [see Fig. 12(b)]. As soon as Pe exceeds this range, the temporal growth rate no longer attenuates but eventually enhances with Pe [see Fig. 12(d)], and ultimately the maximum value of the temporal growth rate approaches a saturation value $kc_{imax} = 1.596 \times 10^{-4}$ approximately. In this case, the maximum temporal growth rate does not disappear from the unstable zone with the increasing value of the Péclet number. This fact is fully consistent with the results reported in Figs. 12(a) and 12(c) respectively. Therefore, one can conclude that the Péclet number has stabilizing as well as destabilizing roles on the shear mode.

F. Competition between surface and shear modes

In this section, we shall focus on the competition between shear and surface modes as discussed by De Bruin [10]. In fact, the surface and shear modes compete with each other to dominate the primary instability when the inclination angle is quite small. In order to explore this physical phenomenon in the presence of slippery wall and surface surfactant, the numerical experiment is performed again for a water flow with $\theta = 3'$, Ka $= 35\,548.25$ [12]. In the first case, we vary the slip length while the Marangoni number is set to zero. The results are displayed in Fig. 13(a). It is noticed that the surface mode initially dominates the primary instability. As soon as the Reynolds number corresponding to the shear mode exceeds the critical Reynolds number ($\mathrm{Re_c} = 3800$ approximately at $\beta = 0$), the shear mode appears in the neutral diagram along with the surface mode to control the primary instability. Further, the unstable region increases corresponding to the surface mode but decreases corresponding to the shear mode with the increasing value of the slip length. Therefore, in this case, the shear mode has no chance to dominate the

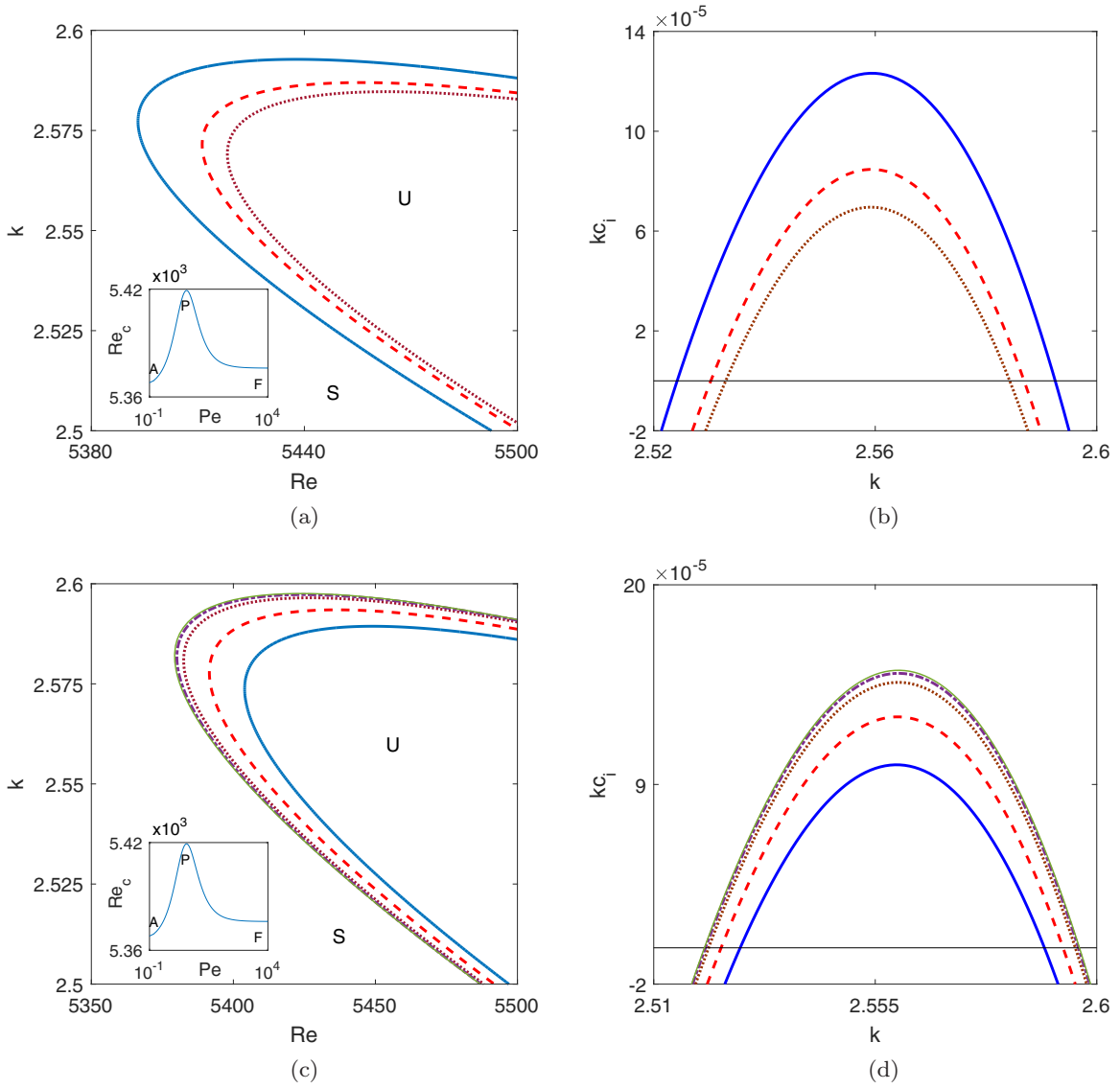

FIG. 12. (a) The variation of the neutral curve for the shear mode in the (Re, k) plane for different values of the Péclet number when $\theta = 1'$, Ma $= 1$, Ca $= 2$, and $\beta = 0$. Solid, dashed, and dotted lines stand for Pe $= 1$, Pe $= 2$, and Pe $= 3$, respectively. (b) The variation of the temporal growth rate kc_i for the shear mode with the wave number k when Re $= 5450$. Solid, dashed, and dotted lines stand for Pe $= 1$, Pe $= 2$, and Pe $= 3$, respectively. (c) The variation of the neutral curve for the shear mode in the (Re, k) plane for different values of the Péclet number when $\theta = 1'$, Ma $= 1$, Ca $= 2$, and $\beta = 0$. Solid, dashed, dotted, dash-dotted, and thin lines stand for Pe $= 10$, Pe $= 20$, Pe $= 50$, Pe $= 80$, and Pe $= 100$, respectively. (d) The variation of the temporal growth rate kc_i for the shear mode with the wave number k when Re $= 5450$. Solid, dashed, dotted, dash-dotted, and thin lines stand for Pe $= 10$, Pe $= 20$, Pe $= 50$, Pe $= 80$, and Pe $= 100$, respectively. Here "U" and "S" indicate unstable and stable regions, respectively.

primary instability by competing with the surface mode. In addition, the current result is verified with that of Floryan *et al.* [12] at $\beta = 0$, and an excellent agreement is achieved. If the inclination angle is switched to $\theta = 0.25'$ in the numerical experiment, the shear mode dominates the primary instability rather than the surface mode [see Fig. 13(b)]. However, as soon as the Reynolds number corresponding to the surface mode crosses the critical Reynolds number ($\mathrm{Re_c} = 17\,188$ approximately at $\beta = 0$), the surface mode appears in the neutral diagram along with the shear mode to control the primary instability. In this case also, the unstable region increases corresponding to the surface mode [see inset of Fig. 13(b)] but decreases corresponding to the shear mode with the increasing value of the slip length. Consequently, the surface mode may dominate the primary instability as the slip length increases gradually. There is evidence that the surface mode dominates the primary instability at $\beta = 0.03$, which is demonstrated by a dash-dotted line in Fig. 13(b). In this case, the critical Reynolds number ($\mathrm{Re_c} = 16\,668$ approximately at $\beta = 0.03$) of the surface mode is lower than the critical Reynolds number of the shear mode ($\mathrm{Re_c} = 19\,313$ approximately at $\beta = 0.03$). Therefore, for each inclination angle, we can find out a slip length for which the critical Reynolds numbers corresponding to the shear and surface modes are equal, which can be found in Fig. 13(c). In other words, we can recognize a phase boundary in the plane of inclination angle and slip

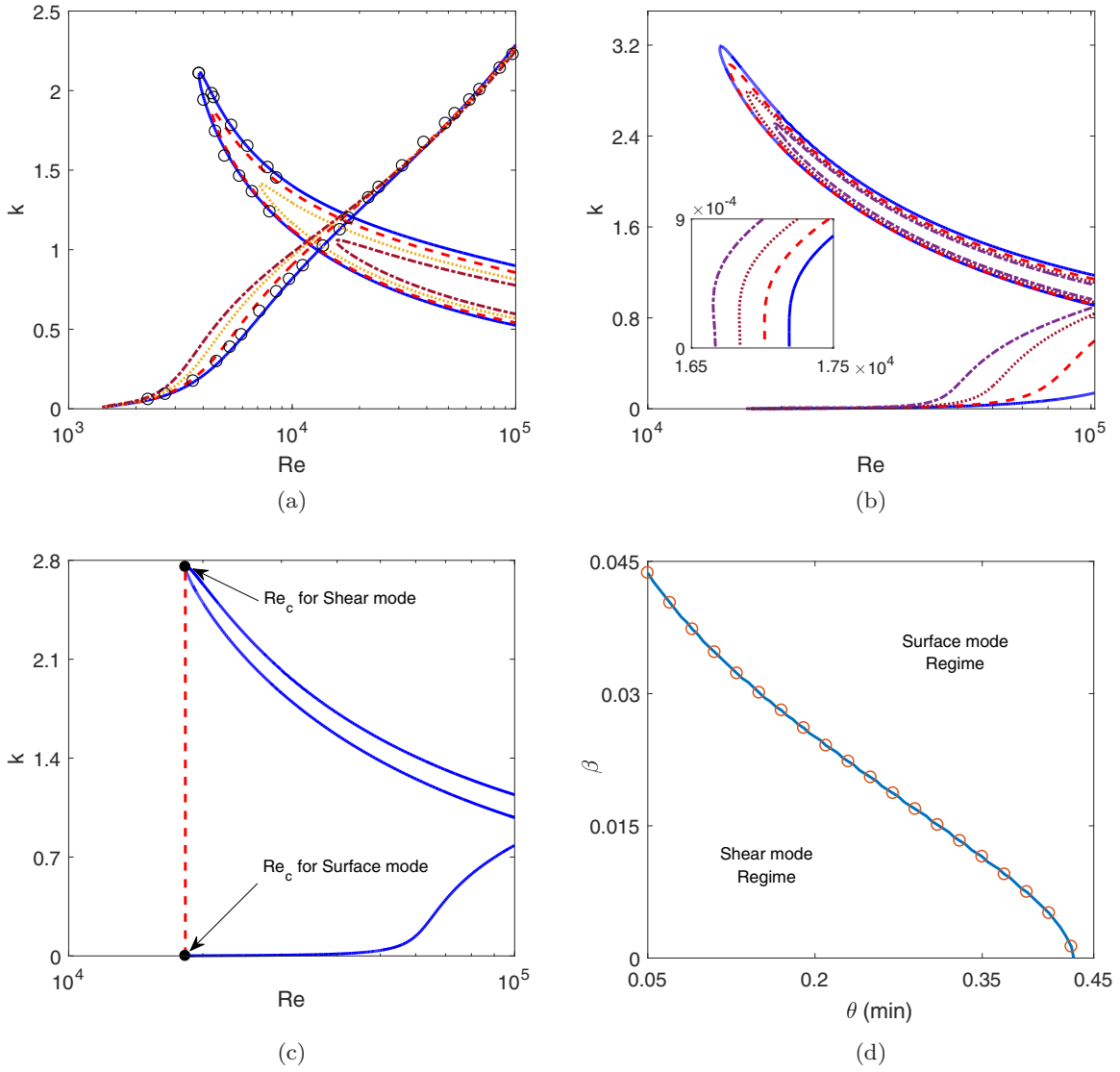

FIG. 13. (a) The variation of the neutral curves for the surface and shear modes in the (Re, k) plane for different values of the slip length when $\theta = 3'$, Ka $= 35\,548.25$, and Ma $= 0$. Solid, dashed, dotted, and dash-dotted lines stand for $\beta = 0$, $\beta = 0.01$, $\beta = 0.02$, and $\beta = 0.03$, respectively. The circles are results of Floryan *et al.* [12]. (b) The variation of the neutral curves for the surface and shear modes in the (Re, k) plane for different values of the slip length when $\theta = 0.25'$, Ka $= 81\,385.18$, and Ma $= 0$. Solid, dashed, dotted, and dash-dotted lines stand for $\beta = 0$, $\beta = 0.01$, $\beta = 0.02$, and $\beta = 0.03$, respectively. (c) The critical Reynolds numbers $\mathrm{Re_c}$ corresponding to the surface and shear modes. (d) The phase boundary between the surface and shear modes.

length, that demarcates the regimes of the surface and shear modes. The result is depicted in Fig. 13(d). Therefore, if we select parameters above the boundary, the surface mode will dominate the primary instability. Otherwise, the shear mode will trigger the primary instability once the parameters are chosen below the boundary.

In the second case, we vary the Marangoni number while the slip length is set to zero. The results are displayed in Fig. 14(a) for a water flow with $\theta = 1'$, Ka $= 51\,269.45$ [12]. Obviously, the surface mode dominates the primary instability at the beginning of the numerical experiment. As soon as the Reynolds number corresponding to the shear mode is beyond its critical value ($\mathrm{Re_c} = 5990$ approximately at Ma $= 0$), the shear mode appears in the neutral diagram along with the surface mode to control the primary instability. In this case, the unstable region decreases corresponding to both surface and shear modes with the increasing value of the Marangoni number [see inset of Fig. 14(a)]. However, the effect of the Marangoni number on the surface mode is more prominent than that on the shear mode. As a consequence, the shear mode may get a chance to dominate the primary instability by competing with the surface mode. For this reason, we continue to increase the Marangoni number. It is observed that the shear mode dominates the primary instability at Ma $= 10$ because in this case, the critical Reynolds number ($\mathrm{Re_c} = 7468$ approximately at Ma $= 10$) of the surface mode is higher than the critical Reynolds number of the shear mode ($\mathrm{Re_c} = 6423$ approximately at Ma $= 10$). The result is demonstrated by a dash-dotted line in Fig. 14(a). Furthermore, if the inclination angle is reduced to $\theta = 0.25'$ as in the previous case, the shear mode dominates the primary instability rather than the surface mode [see Fig. 14(b)]. However, as soon as the Reynolds

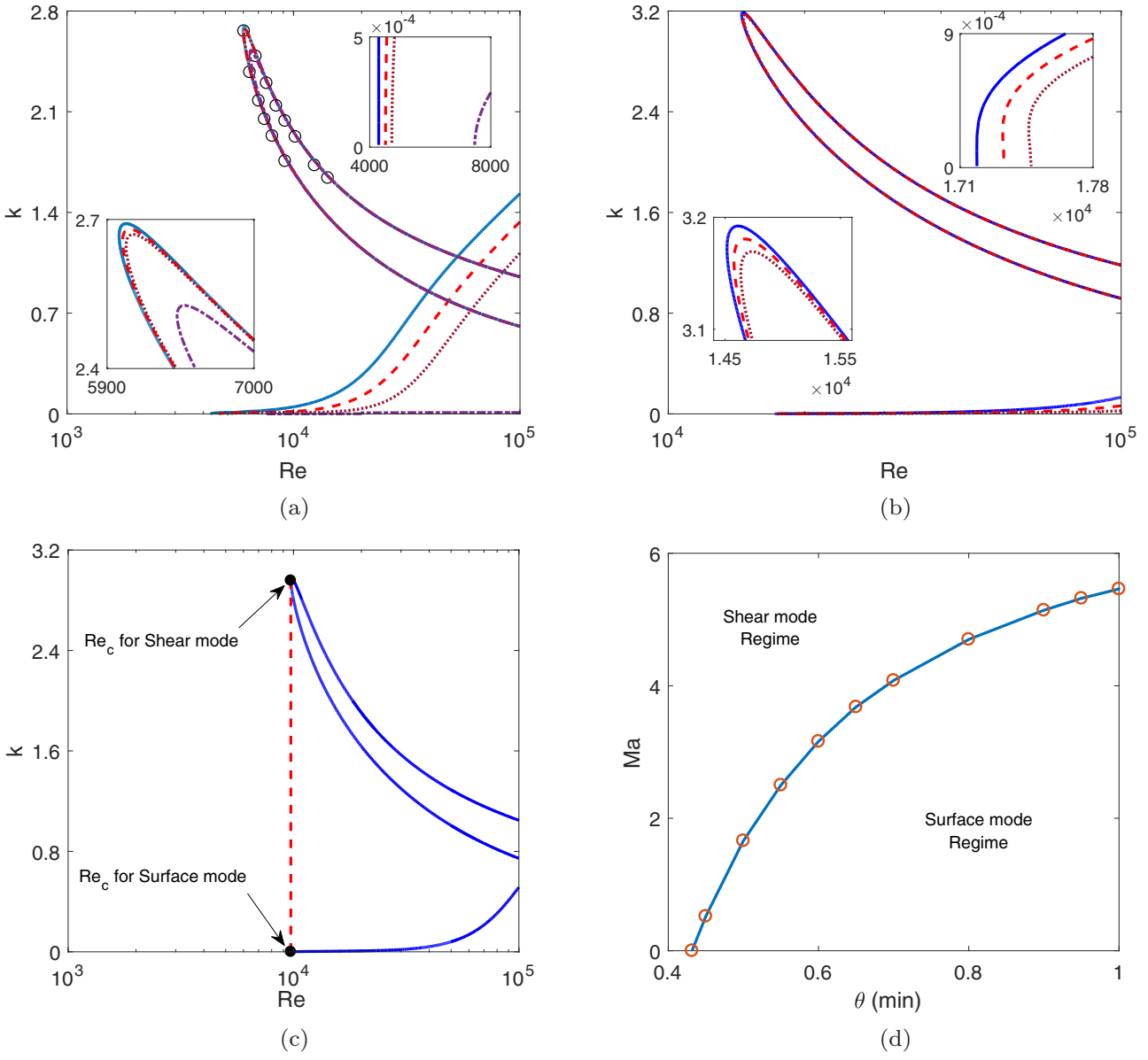

FIG. 14. (a) The variation of the neutral curves for the surface and shear modes in the (Re, k) plane for different values of the Marangoni number when $\theta = 1'$, Ka $= 51\,269.45$, and $\beta = 0$. Solid, dashed, dotted, and dash-dotted lines stand for Ma $= 0$, Ma $= 0.5$, Ma $= 1$, and Ma $= 10$, respectively. The circles are results of Floryan *et al.* [12]. (b) The variation of the neutral curves for the surface and shear modes in the (Re, k) plane for different values of the Marangoni number when $\theta = 0.25'$, Ka $= 81\,385.18$, and $\beta = 0$. Solid, dashed, and dotted lines stand for Ma $= 0$, Ma $= 0.5$, and Ma $= 1$, respectively. (c) The critical Reynolds numbers Re$_c$ corresponding to the surface and shear modes. (d) The phase boundary between the surface and shear modes.

number crosses the critical Reynolds number (Re$_c = 17\,188$ approximately at Ma $= 0$) corresponding to the surface mode, the surface mode appears in the neutral diagram along with the shear mode to control the primary instability. The unstable region decreases corresponding to both surface and shear modes with the increasing value of the Marangoni number [see inset of Fig. 14(b)]. In addition, the effect of the Marangoni number on the surface mode is significant in comparison with the shear mode. Therefore, in this case, the surface mode does not have any chance to dominate the primary instability by competing with the shear mode because the critical Reynolds number of the shear mode is always lower than the critical Reynolds number of the surface mode with the increasing value of the Marangoni number. Unlike the previous case, for each inclination angle there exists a Marangoni number such that the critical Reynolds numbers corresponding to the shear and surface modes are equal, which can be found in Fig. 14(c). Therefore, in this case also, we can recognize a phase boundary in the plane of the inclination angle and the Marangoni number, that demarcates the regimes of the surface and shear modes. The result is depicted in Fig. 14(d). Hence, if the parameters are selected above the boundary, the shear mode will drive the primary instability. Otherwise, the surface mode will drive the primary instability once the parameters are chosen below the boundary.

V. INVISCID STABILITY ANALYSIS WITHOUT SURFACTANT

In order to figure out the stabilizing effect of slip length on the unstable shear wave at sufficiently large Reynolds number as well as at sufficiently small inclination angle, the OS BVP (37)–(42) is also tackled analytically. To do that, we first introduce a new parameter $\mathrm{We} = \sigma_0/(\rho U_s^2 d) = 1/(\mathrm{CaRe})$, where We, the Weber number, shows the effect of surface tension. In the inviscid limiting approximation ($\mathrm{Re} \to \infty$, or equivalently, $\mu \to 0$), the fourth-order OS BVP (37)–(42) simplifies into a second-order boundary value problem

$$[(U-c)(\partial_{yy} - k^2) - \partial_{yy}U]\phi = 0, \tag{78}$$

$$\phi = 0 \ \text{ at } \ y = 0, \tag{79}$$

$$[(U-c)^2\partial_y - 2\cot\theta/\{\mathrm{Re}(1+2\beta)\} - \mathrm{We}\,k^2]\phi = 0 \ \text{ at } \ y = 1, \tag{80}$$

where $c = c_r + ic_i$ is the complex wave speed. Note that the term $2\cot\theta/\{\mathrm{Re}(1+2\beta)\}$ is retained in the normal stress balance equation (80) due to the assumption of a very small inclination angle ($\theta \to 0$), which makes that term finite and therefore non-negligible. In accordance with Howard [45], Floryan *et al.* [12], and Samanta [42], we apply the transformation $\phi = (U-c)\Phi$, that converts the second-order BVP (78)–(80) into the following form:

$$\partial_y[(U-c)^2\partial_y\Phi] - (U-c)^2k^2\Phi = 0, \tag{81}$$

$$\Phi(0) = 0, \tag{82}$$

$$[(U-c)^2\partial_y - 2\cot\theta/\{\mathrm{Re}(1+2\beta)\} - k^2\mathrm{We}]\Phi(1) = 0. \tag{83}$$

Multiplying by complex conjugate Φ^* with (81), integrating with respect to y over the liquid layer domain [0, 1], and using the boundary conditions (82) and (83), finally we obtain

$$\int_0^1 (U - c_r - ic_i)^2 Q \, dy = [2\cot\theta/\{\mathrm{Re}(1+2\beta)\} + k^2\mathrm{We}]|\Phi(1)|^2, \tag{84}$$

where $Q = (|\partial_y\Phi|^2 + k^2|\Phi|^2) \geqslant 0$. Comparing the real and imaginary parts from both sides of (84), we can write

$$\int_0^1 \left[(U-c_r)^2 - c_i^2\right] Q \, dy = [2\cot\theta/\{\mathrm{Re}(1+2\beta)\} + k^2\mathrm{We}]|\Phi(1)|^2 \tag{85}$$

and

$$c_i \int_0^1 (U - c_r) Q \, dy = 0. \tag{86}$$

As we are interested in deciphering the unstable shear mode ($c_i > 0$), integral (86) will not vanish for $c_r > 1$ unless $\Phi(y) = 0$, which implies the existence of a trivial solution. Thus, for a nontrivial solution, one can predict that there does not exist unstable shear mode for $c_r > 1$. On the contrary, for $c_r < 1$, there is a possibility of the existence of the unstable shear mode, whose phase speed is given by

$$c_r = 1 - \left\{\frac{\int_0^1 (1-y)^2 Q \, dy}{(1+2\beta)\int_0^1 Q \, dy}\right\}. \tag{87}$$

Obviously, the phase speed increases in the presence of the slippery wall. Inserting the expression of c_r into Eq. (85) and after doing some mathematical manipulation, we get

$$c_i^2 = \frac{1}{(1+2\beta)^2}\left[\frac{\int_0^1 (1-y)^4 Q \, dy}{\int_0^1 Q \, dy} - \left\{\frac{\int_0^1 (1-y)^2 Q \, dy}{\int_0^1 Q \, dy}\right\}^2\right] - \frac{[2\cot\theta/\{\mathrm{Re}(1+2\beta)\} + k^2\mathrm{We}]|\Phi(1)|^2}{\int_0^1 Q \, dy}. \tag{88}$$

Expression (88) shows that for a given fluid, c_i^2, or equivalently, the growth rate for the shear mode attenuates with the increasing value of the slip length at a sufficiently small inclination angle. This result is fully consistent with the stabilizing influence of slip length on the shear mode reported in Sec. IV C.

VI. CONCLUSIONS

A viscous incompressible gravity-driven fluid flow down a slippery inclined plane is investigated in the presence of an insoluble surface surfactant. The linear stability analysis is performed for infinitesimal disturbances of arbitrary wave numbers based on the Orr-Sommerfeld boundary value problem. The surface and shear modes are analyzed in detail for different values of the flow parameters. The long-wave analysis predicts that there exist surface and surfactant modes. The wall slip destabilizes the surface mode in the vicinity of the threshold of instability by decreasing the critical Reynolds number. On the contrary, the insoluble surface surfactant stabilizes the surface mode in the vicinity of the threshold by increasing the critical Reynolds number. Further, the long-wave analysis predicts that the surfactant mode is always stable at low Reynolds number.

Far from the threshold of instability, the Orr-Sommerfeld boundary value problem is resolved by using the Chebyshev spectral collocation method for infinitesimal disturbances of arbitrary wave numbers, or equivalently, of arbitrary Reynolds numbers. In the long-wave regime, the numerical results capture the analytical results accurately for different values of the flow parameters. It is noteworthy to point out that the wall slip demonstrates an opposite effect, i.e., a stabilizing effect on the surface mode in the finite wave-number regime. However, the insoluble surfactant demonstrates a stabilizing effect on the surface mode in the finite wave-number regime as the result of the long-wave regime. Further, it is observed that the Péclet number demonstrates a dual role on the surface mode, i.e., the unstable region increases in the vicinity of the critical Reynolds number but decreases far from the critical Reynolds number as soon as the Péclet number increases.

If the Reynolds number is increased in the numerical experiment, the shear mode is identified along with the surface mode. However, in this case, the inclination angle should be sufficiently small to detect the shear mode. It is noticed that the shear mode is stabilized by both wall slip and insoluble surfactant. However, the impact of slip length on the shear

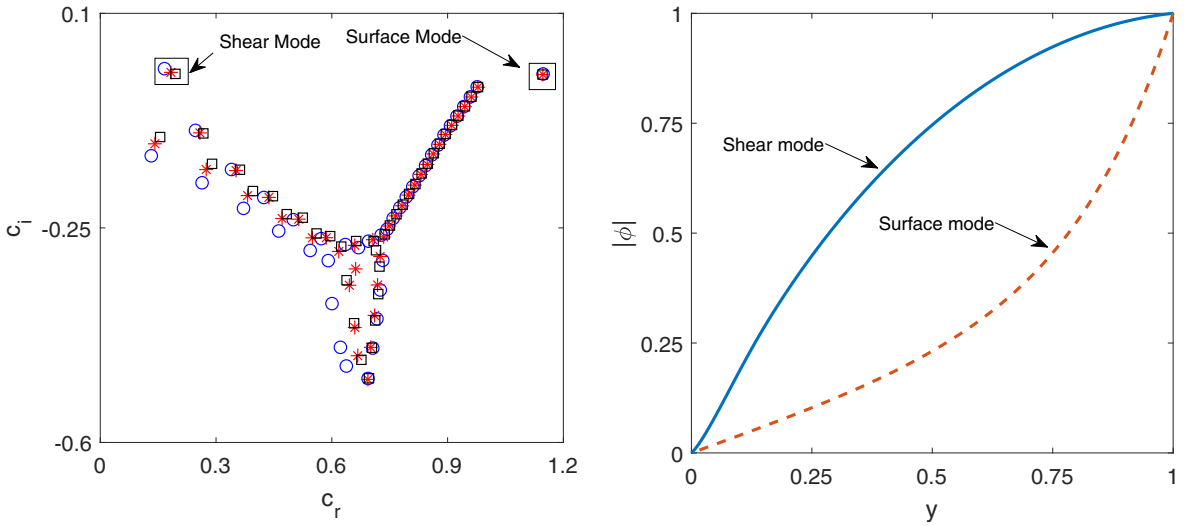

FIG. 15. (a) The spectrum of the eigenvalue problem (75) for different values of the slip length when $k = 0.9$, $\mathrm{Re} = 30\,000$, $\theta = 3'$, $\mathrm{Ka} = 35\,548.25$, and $\mathrm{Ma} = 0$. Here circles, stars, and squares represent the results of $\beta = 0$, $\beta = 0.02$, and $\beta = 0.03$, respectively. (b) The variation of the absolute value of the normalized eigenfunction $|\phi|$ as a function of y when $\beta = 0.02$. The solid and dashed lines represent the eigenfunctions corresponding to the shear and surface modes, respectively.

mode is more prominent than the Marangoni number. It is noteworthy to point out that the Péclet number exhibits a dual behavior on the shear mode as in the case of the surface mode. However, the result corresponding to the shear mode is opposite to that of the surface mode, i.e., the Péclet number initially shows a stabilizing effect in the range $[0, 3.5]$ but eventually, it shows a destabilizing effect as soon as the Péclet number crosses the upper limit. Further, it is noticed that both surface and shear modes are competing with each other to dominate the primary instability when the inclination angle is sufficiently small. Therefore, it is possible to find out exact parameter values for which the critical Reynolds numbers corresponding to the surface and shear modes are the same. In other words, new phase boundaries are recognized in the regimes of flow parameters that separate the domains of shear and surface modes.

ACKNOWLEDGMENTS

A.S. acknowledges the support from SERB (ECR/2017/000264), Department of Science and Technology, Government of India.

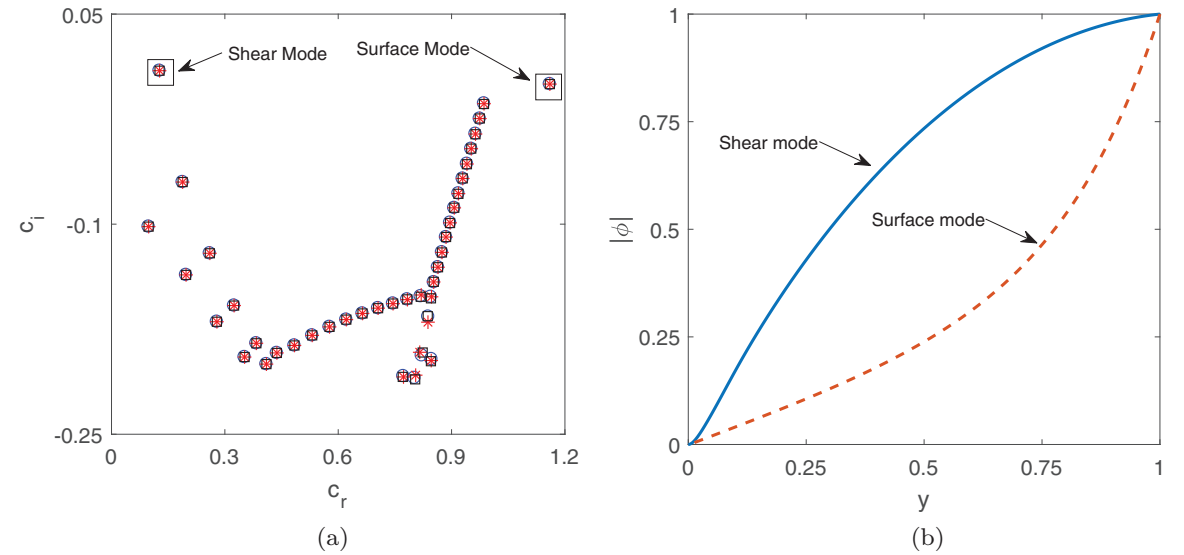

FIG. 16. (a) The spectrum of the eigenvalue problem (75) for different values of the slip length when $k = 0.8$, $\mathrm{Re} = 80\,000$, $\theta = 1'$, $\mathrm{Ka} = 51\,269.4$, and $\beta = 0$. Here circles, stars, and squares represent the results of $\mathrm{Ma} = 0$, $\mathrm{Ma} = 0.5$, and $\mathrm{Ma} = 1$, respectively. (b) The variation of the absolute value of the normalized eigenfunction $|\phi|$ as a function of y when $\mathrm{Ma} = 1$. The solid and dashed lines represent the eigenfunctions corresponding to the shear and surface modes, respectively.

APPENDIX: SPECTRUM OF THE ORR-SOMMERFELD EIGENVALUE PROBLEM

In order to reveal the surface and shear modes simultaneously in the high Reynolds number regime, the full spectrum is depicted for two different cases. In the first case, we vary the slip length while the Marangoni number is fixed (Ma = 0). The result is shown in Fig. 15(a) for a water flow with $\theta = 3'$, Ka = 35 548.25 [12]. Indeed, the surface and shear modes appear in the spectrum because the Reynolds number is selected from the regime where both modes are unstable. Figure 15(b) demonstrates the absolute value of the normalized eigenfunctions corresponding to the surface and shear modes when $\beta = 0.02$. In the second case, the Marangoni number is varied while the slip length is kept constant ($\beta = 0$). The result is illustrated in Fig. 16(a) for a water flow with $\theta = 1'$, Ka = 51 269.4 [12]. In this case also, the surface and shear modes appear in the spectrum because the Reynolds number belongs to the zone where both modes are unstable. Figure 16(b) demonstrates the absolute value of the normalized eigenfunctions corresponding to the surface and shear modes when Ma = 1.

[1] P. L. Kapitza, *Collected Papers of P. L. Kapitza* (Pergamon, New York, 1965).
[2] S. J. Weinstein and K. J. Ruschak, Annu. Rev. Fluid Mech. **36**, 29 (2004).
[3] N. Brauner and D. M. Maron, Int. J. Heat Mass Transfer **25**, 99 (1982).
[4] N. A. Malamataris, M. Vlachogiannis, and V. Bontozoglou, Phys. Fluids **14**, 1082 (2002).
[5] H. C. Chang and E. A. Demekhin, *Complex Wave Dynamics on Thin Films* (Elsevier, New York, 2002).
[6] S. Kalliadasis, C. Ruyer-Quil, B. Scheid, and M. G. Velarde, *Falling Liquid Films* (Springer, New York, 2012).
[7] T. B. Benjamin, J. Fluid Mech. **2**, 554 (1957).
[8] C. S. Yih, Phys. Fluids **6**, 321 (1963).
[9] S. P. Lin, Phys. Fluids **10**, 308 (1967).
[10] G. J. De Bruin, J. Eng. Math. **8**, 259 (1974).
[11] R. W. Chin, F. H. Abernathy, and J. R. Bertschy, J. Fluid Mech. **168**, 501 (1986).
[12] J. M. Floryan, S. H. Davis, and R. E. Kelly, Phys. Fluids **30**, 983 (1987).
[13] O. I. Vinogradova, Langmuir **11**, 2213 (1995).
[14] T. D. Blake, Colloids Surf. **47**, 135 (1990).
[15] C. Neto, D. R. Evans, E. Bonaccurso, H. J. Butt, and V. S. J. Craig, Rep. Prog. Phys. **68**, 2859 (2005).
[16] G. S. Beavers and D. D. Joseph, J. Fluid Mech. **30**, 197 (1967).
[17] S. Whitaker, *The Method of Volume Averaging* (Kluwer, Dordrecht, 1999).
[18] J. P. Pascal, J. Phys. D: Appl. Phys. **32**, 417 (1999).
[19] M. Sadiq and R. Usha, Phys. Fluids **20**, 022105 (2008).
[20] U. Thiele, B. Goyeau, and M. G. Velarde, Phys. Fluids **21**, 014103 (2009).
[21] A. Samanta, C. Ruyer-Quil, and B. Goyeau, J. Fluid Mech. **684**, 353 (2011).
[22] S. Whitaker and L. O. Jones, AIChE **12**, 421 (1966).
[23] W. Ji and F. Setterwall, J. Fluid Mech. **278**, 297 (1994).
[24] C. Pozrikidis, J. Fluid Mech. **496**, 105 (2003).
[25] M. G. Blyth and C. Pozrikidis, J. Fluid Mech. **521**, 241 (2004).
[26] H. H. Wei, Phys. Fluids **17**, 012103 (2005).
[27] H. H. Wei, Phys. Rev. E **75**, 036306 (2007).
[28] G. Karapetsas and V. Bontozoglou, J. Fluid Mech. **729**, 123 (2013).
[29] G. Karapetsas and V. Bontozoglou, J. Fluid Mech. **741**, 139 (2014).
[30] Anjalaiah, R. Usha, and S. Millet, Phys. Fluids **25**, 022101 (2013).
[31] R. S. Voronov, D. V. Papavassiliou, and L. L. Lee, Ind. Eng. Chem. Res. **47**, 2455 (2008).
[32] A. A. Nepomnyashchy, M. G. Velarde, and P. Colinet, *Interfacial Phenomena and Convection* (Chapman and Hall/CRC, Boca Raton, 2002).
[33] A. L. Frenkel and D. Halpern, Phys. Fluids **14**, L45 (2002).
[34] D. Halpern and A. L. Frenkel, J. Fluid Mech. **485**, 191 (2003).
[35] D. Halpern and A. L. Frenkel, J. Fluid Mech. **594**, 125 (2008).
[36] A. Samanta, Phys. Fluids **26**, 094105 (2014).
[37] A. Samanta, Phys. Fluids **29**, 094103 (2017).
[38] A. Samanta, Phys. Lett. A **372**, 6653 (2008).
[39] P. J. Schmid and D. S. Henningson, *Stability and Transition in Shear Flows* (Springer, New York, 2001).
[40] S. A. Orszag, J. Fluid Mech. **50**, 689 (1971).
[41] J. J. Dongarra, B. Straughan, and D. W. Walker, Appl. Numer. Math. **22**, 399 (1996).
[42] A. Samanta, Phys. Rev. E **88**, 053002 (2013).
[43] M. G. Blyth and C. Pozrikidis, J. Fluid Mech. **505**, 59 (2004).
[44] N. Tilton and L. Cortelezzi, J. Fluid Mech. **604**, 411 (2008).
[45] L. N. Howard, J. Fluid Mech. **10**, 509 (1961).
[46] N. T. Nguyen, *Micromixers: Fundamentals, Design and Fabrication* (William Andrew Inc., Norwich, 2012).
[47] B. E. Rapp, *Microfluidics: Modeling, Mechanics, and Mathematics* (Elsevier, New York, 2017).